

Fast and scalable finite-element based approach for density functional theory calculations using projector-augmented wave method

Kartick Ramakrishnan,¹ Sambit Das,² and Phani Motamarri^{1,*}

¹*Department of Computational and Data Sciences, Indian Institute of Science Bengaluru, India*

²*Department of Mechanical Engineering, University of Michigan, Ann Arbor, Michigan 48109, USA*

(Dated: July 22, 2024)

Gaining *ab initio* insights into complex materials problems involving nanometers in length-scale and nanoseconds of time-scale demand enormous computational resources owing to the stringent accuracy requirements of density functional theory (DFT) calculations compounded with the cubic scaling complexity of DFT with number of atoms. This study presents a new approach that utilizes a local real-space formulation discretized with finite-element (FE) basis to enable rapid and scalable electronic structure calculations employing the projector augmented wave (PAW) method. To achieve this, we have developed efficient computational techniques that leverage emerging computing architectures. These techniques incorporate low-rank perturbation of identity, block-diagonal representation of inverse PAW overlap matrix using spectral finite-element basis, Chebyshev Filtered subspace iteration approach in conjunction with mixed-precision arithmetic to solve the underlying FE discretized PAW generalized eigenproblem. Our framework (PAW-FE) significantly reduces the degrees of freedom compared to norm-conserving pseudopotentials while ensuring the necessary chemical accuracy and accommodating generic boundary conditions, thereby enabling faster and accurate large-scale DFT simulations than possible today. Furthermore, our approach demonstrates a considerable computational advantage over state-of-the-art plane-wave codes for system sizes greater than 3000 electrons. Notably, our framework represents the first real-space PAW approach capable of competing with plane-wave methods. Finally, we illustrate the effectiveness of PAW-FE for addressing large-scale problems involving tens of thousands of electrons, which are beyond the capabilities of existing plane-wave codes.

I. INTRODUCTION

Electronic structure calculations based on Kohn-Sham density functional theory (DFT) have significantly advanced our understanding of material properties. The Kohn-Sham approach to DFT [1, 2] reformulates the many-body problem of interacting electrons into an equivalent computationally tractable problem of non-interacting electrons within an effective mean field governed by electron density. This reformulation has made it possible to predict a wide range of material properties, including mechanical, transport, electronic, magnetic and optical properties, over the past six decades. Pseudopotential approximations in DFT [3–5] have been crucial in making these calculations computationally efficient, as they focus only on valence electrons that participate in chemical bonding. To this end, these approximations transform an all-electron DFT calculation into an equivalent problem involving smooth pseudo-wave-functions for valence electrons, using an effective external potential (pseudopotential) that lumps the effect of core-electrons and the singular Coulomb nuclear potential. In a numerical setting, pseudopotential DFT calculations are computationally efficient since they only compute valence electronic wavefunctions, allowing for the use of coarser grids or lower plane-wave energy cutoffs to resolve these smooth pseudo electronic fields. Over the years, pseudopotentials have evolved from norm-conserving [6–9] to

ultrasoft potentials [10], and now to the state-of-the-art projector augmented wave (PAW) [11] method, enabling accurate predictions of material properties across diverse material systems without the need for expensive all-electron DFT calculations. However, the stringent accuracy required for DFT calculations to compute meaningful properties, combined with the cubic-scaling computational complexity with the number of electrons, demands significant computational resources even for pseudopotential DFT calculations, typically limiting their application to material systems with at most few thousands of electrons. Overcoming the current limits on *ab-initio* calculations has been a decades-long pursuit by researchers around the world, and efforts over the past three decades have focussed on developing accurate and computationally efficient methods for solving the Kohn-Sham DFT problem. These include efficient discretization methods for solving DFT equations, reduced-scaling algorithms for lowering the computational complexity of the DFT problem as well as efforts to improve the parallel scalability of the widely used codes. Among the various discretization methods, plane wave (PW) basis is the most popular method of choice for metallic and heterogenous material systems due to the computational efficiency afforded by these basis sets owing to its spectral convergence. Despite the popularity of PW basis for DFT calculations, the limitations of these Fourier methods stemming from the poor scalability on parallel computing architectures, the inefficiency in treating non-periodic systems, and the inability to handle generic boundary conditions led to the devel-

* phanim@iisc.ac.in

opment of systematically improvable, efficient, and scalable real-space discretization techniques based on finite-difference [12–16], finite-elements [17–30], wavelets [31–33] and other reduced-order basis techniques [34–38].

The finite-element (FE) basis, a compactly supported piece-wise polynomial basis, is a relatively new approach in real-space methods for DFT, offering several advantages over other commonly used basis sets. FE basis sets are systematically convergent for any material system, can accommodate generic boundary conditions including fully periodic, semi-periodic, non-periodic. Their locality allows one to exploit fine-grained parallelism on modern heterogeneous architectures while providing excellent parallel scalability on distributed systems [39, 40]. As demonstrated in previous works [29, 30], finite-element-based methods have significantly outperformed plane-wave basis in the case of norm-conserving pseudopotential DFT calculations, as the system size increases for a given accuracy of ground-state energy and forces. Furthermore, adaptive resolution offered by FE basis sets enables all-electron calculations [23, 27] but mixed all-electron and pseudopotential calculations [27, 41]. The open-source code DFT-FE [42], the workhorse behind the ACM Gordon Bell Prize 2023, inherits these features while incorporating scalable and efficient solvers for the solution of Kohn-Sham equations. The DFT-FE code has shown excellent scalability massively parallel many-core CPU and hybrid CPU-GPU architectures (tested up to 200,000 cores on many-core CPUs and 40,000 GPUs on hybrid CPU-GPU architectures), while simulating material systems as large as 600,000 electrons [30, 40]. Furthermore, DFT-FE has been recently employed in a range of scientific studies involving large-scale DFT calculations on material systems with tens of thousands of electrons – computing the electronic structure of large DNA molecules [43], predicting energetics of extended defects in crystalline materials [30, 40, 44–46], investigating phase transformations in doped nanofilms [47], evaluating spin Hamiltonian parameters of systems with defects [41, 48] and solving inverse DFT problem [49].

We note that the aforementioned finite-element-based DFT calculations are all limited to the use of norm-conserving pseudopotentials. These pseudopotentials can become very hard for material systems with elements involving d or f electrons and these DFT calculations can be computationally demanding. Further, these often require semi-core states to be treated as valence states for better transferability, resulting in harder pseudopotentials with more valence electrons, particularly for alkali, alkaline earth metals, or early transition metals. Previous works [29, 42] have shown that these hard norm-conserving pseudopotentials require a large number of degrees of freedom (30,000 to 50,000 finite-element basis functions per atom) to achieve chemical accuracy, leading to high computational costs for solving the Kohn-Sham DFT eigenvalue problem. While ultrasoft pseudopotentials relax the norm conservation condition [7], resulting in softer potentials, their construction is complex and re-

quires extensive testing to ensure accuracy and transferability. To address these issues, Blöchl [11] developed the projector augmented wave (PAW) method, formally an all-electron approach that generalizes the LAPW method and the pseudopotential approach. The PAW method recovers all-electron wavefunctions by introducing a linear transformation operator (\mathcal{T}) acting on smoothly varying pseudo wavefunctions. Within the frozen core approximation, it treats core states as frozen and retrieves the oscillatory behavior of all-electron valence wavefunctions near atomic centers through the action of \mathcal{T} on the smooth pseudo-valence wavefunctions. This allows one to reformulate the all-electron Kohn-Sham DFT eigenproblem into an equivalent PAW eigenvalue problem involving only smooth pseudo-valence wavefunctions, striking a balance between accuracy and computational efficiency. As a result, the PAW approach within the frozen core approximation has become widely adopted in popular plane-wave based DFT codes [50–55].

The real-space discretization techniques have also been employed in the context of PAW implementations and are primarily based on finite-difference approximations [56, 57], wavelet based methods [58] and psinc basis [59]. However, most of these PAW based DFT calculations deal with material systems involving few thousands of electrons excepting the linear scaling DFT approach [59] using the PAW method applied to material systems with a band-gap. The computational efficiency and scalability of these real-space implementations compared to state-of-the-art plane-wave-based PAW implementations remains unknown. This work introduces the local real-space formulation of the PAW method amenable for finite-element (FE) discretization, proposing efficient strategies to solve the underlying FE-discretized PAW generalized eigenvalue problem using a self-consistent field iteration approach. Our methodology significantly reduces FE degrees of freedom required to achieve chemical accuracy using the PAW method, outperforming the optimized norm-conserving (ONCV) pseudopotential based DFT calculations employed in previous FE based approaches for a given system size. Additionally, we demonstrate that our method can handle fully periodic, non-periodic, and semi-periodic boundary conditions for generic material systems as large as 50,000 electrons, offering substantial computational efficiencies over state-of-the-art plane-wave-based approaches for systems with over 5,000 electrons and being competitive for systems with around 3,000 electrons. Notably, to the best of our knowledge this represents the first development of a fast and scalable approach for the PAW method within the framework of finite-element discretization.

We adopt the original Blöchl’s [11] PAW method in our current work and do not employ the Kresse’s modifications [50] that include the compensation charge contribution for computing the exchange-correlation term, which increases computational costs and introduces numerical instabilities [51, 52]. The key aspects of the proposed finite-element (FE) approach for the PAW method

include: (i) local reformulation of the extended PAW electrostatics involving smooth pseudo-electron density and the compensation charge making it amenable for FE discretization; (ii) deducing the discretised governing equations by evaluating the variational derivative of the locally reformulated all-electron DFT energy functional in the PAW method; (iii) employing higher-order quadrature rules to efficiently and accurately evaluate integrals involving atom-centered functions, allowing the use of coarser FE grids for electronic fields and yet capture the relevant PAW atomic data; (iv) implementation of a self-consistent field (SCF) iteration approach based on Anderson mixing of total charge density using an efficient real-space strategy to minimize the weighted total charge density residual norm; (v) an efficient scheme to evaluate the inverse of FE discretized PAW overlap matrix \mathbf{S} using Woodbury's formula in conjunction with Gauss-Lobatto-Legendre quadrature rules and a block-wise matrix inversion for the overlap of atomic projectors in real-space; and (vi) leveraging this efficient computation of \mathbf{S}^{-1} to design a Chebyshev polynomial based filter [60] in each SCF iteration to compute the space rich in occupied eigenstates, and solving the PAW generalized eigenvalue problem by projecting onto this filtered space. The proposed formulation has been implemented in a distributed setting on CPUs using the message passing interface (MPI) for communication across multiple nodes to enable large-scale PAW based DFT calculations. We benchmark the accuracy and performance of our method against plane-wave-based PAW implementations on various representative non-periodic, semi-periodic, and fully periodic systems. Compared to reference data from plane-wave calculations, our results show excellent agreement in ground-state energies, energy variation with bond length and lattice parameters, formation energies, surface energies, and band structures. Relative to widely used plane-wave based PAW implementations, our finite-element based approach demonstrates significant computational advantage both in terms of CPU node-hrs and minimum wall time with increasing systems sizes reaching up to $5\times$ and $10\times$, respectively, for non-periodic systems ($\sim 18,000$ electrons) and $3\times$ and $6\times$, respectively, for periodic systems ($\sim 34,000$ electrons). Our implementation also exhibits excellent parallel scaling efficiency ($\sim 70\%$) at 1200 degrees of freedom per MPI rank for material systems, achieving nearly a 10-fold speed-up over the state-of-the-art DFT-FE code using norm-conserving ONCV pseudopotentials for system sizes close to 50,000 electrons, with a significant reduction in computational resource requirements.

The remaining sections of the manuscript is organised as follows. Section II briefly introduces the Blöchl PAW method followed by a discussion on the local real-space formulation of the PAW method and the governing equations to be solved. Subsequently, Sec. III introduces the finite-element discretization for the PAW governing differential equations and Sec. IV details the proposed computational methodology in achieving an efficient

and scalable solution procedure for solving the FE discretized PAW generalised eigenvalue problem using a self-consistent field iteration approach. Section V presents comprehensively accuracy and performance benchmarks of our implementation comparing with state of the art PAW based plane-wave(PW) codes on representative benchmark systems. Additionally, this section presents a comparative study of the current work and the norm-conserving pseudopotential (ONCV) in the DFT-FE code in terms of parallel scalability and time to solution. Finally, we conclude with a short discussion summarizing the key findings and outline future prospects arising from this work in Sec. VI

II. REAL-SPACE FORMULATION OF PROJECTOR AUGMENTED WAVE METHOD

The ground-state properties of a material system comprising of N_a nuclei and N_e electrons is governed by the following all-electron Kohn-Sham DFT energy functional [61, 62]

$$E[\{\psi_i\}, \{\mathbf{R}^a\}] = T_s[\{\psi_i\}] + E_{xc}[n(\mathbf{x})] + J[\rho(\mathbf{x}), \{\mathbf{R}^a\}] \quad (1)$$

where $\{\psi_i\}$ and $\{\mathbf{R}^a\}$ denote the set of single-electron orthonormal wavefunctions and the set of nuclear position vectors respectively. We restrict our discussion here to spin-unpolarized case, while the extension to spin-polarized systems is straightforward and not elaborated here.

The term $T_s[\{\psi_i\}]$ in Eq. (1) denotes the kinetic energy of the non-interacting electrons where

$$T_s[\{\psi_i\}] = 2 \sum_i f_i \int \psi_i^*(\mathbf{x}) \left(-\frac{1}{2} \nabla^2 \right) \psi_i(\mathbf{x}) d\mathbf{x}, \quad (2)$$

while $E_{xc}[n(\mathbf{x})]$ is the exchange-correlation energy that accounts for the quantum-mechanical many-body effects. Adopting the generalized gradient approximation (GGA) [63–65] for the exchange-correlation functional description in this work, we have

$$E_{xc}[n(\mathbf{x})] = \int \epsilon_{xc}[n(\mathbf{x}), \nabla n(\mathbf{x})] d\mathbf{x}. \quad (3)$$

where $n(\mathbf{x}) = 2 \sum_i^N f_i |\psi_i(\mathbf{x})|^2$ represents the all-electron density with f_i denoting the orbital occupancy function and the integer $N \geq N_e/2$ denotes the number of single-electron wavefunctions. The total electrostatic energy in Eqn. (1) is denoted by $J[\rho(\mathbf{x}), \{\mathbf{R}^a\}] = E_{el}[\rho(\mathbf{x}), \{\mathbf{R}^a\}] - E_{self}[\{\mathbf{R}^a\}]$. Here, E_{el} is the electrostatics energy associated with the total charge $\rho(\mathbf{x}) = n(\mathbf{x}) + \sum_a b^a(\mathbf{x})$, where $b^a(\mathbf{x}) = -Z^a \delta(\mathbf{x} - \mathbf{R}^a)$ denotes the nuclear charge density with Z^a being the atomic number of a^{th} atom. This electrostatics energy E_{el} involves a convolution in real-space given by:

$$E_{el}[\rho, \{\mathbf{R}^a\}] = \frac{1}{2} \int \int \frac{\rho(\mathbf{x})\rho(\mathbf{y})}{|\mathbf{x} - \mathbf{y}|} d\mathbf{x} d\mathbf{y} \quad (4)$$

where the domain of integration for \mathbf{y} in the above Eqn. (4) is \mathbb{R}^3 , while the domain of integration for \mathbf{x} in the case of an infinite-periodic system is over the unit-cell of interest, whereas in the case of a finite system, it is over \mathbb{R}^3 . Further, for a periodic system the index a refers to atoms at all lattice sites with the compact support of $b^a(\mathbf{x})$ lying in the unit cell of interest, while for a finite system, it refers to all the atoms in the system. Finally, the self-interaction energy corresponding to the nuclear charge density $b^a(\mathbf{x})$ is denoted as $E_{\text{self}}^a[\mathbf{R}^a]$ and hence the total self-interaction energy is given by $E_{\text{self}}[\{\mathbf{R}^a\}] = \sum_a E_{\text{self}}^a[\mathbf{R}^a]$.

Within the frozen-core approximation of PAW formalism, the valence all-electron Kohn-Sham (KS) wavefunctions ($\{\psi_i\}$) that are orthogonal to the core wavefunctions are recovered from pseudo-smooth(PS) wavefunctions ($\{\tilde{\psi}_i\}$) using a linear transformation operator (\mathcal{T}) [11] given by:

$$|\psi_i\rangle = \mathcal{T} |\tilde{\psi}_i\rangle = (\mathcal{I} + \sum_a \mathcal{T}^a) |\tilde{\psi}_i\rangle \quad (5)$$

The index $i = \{1, 2, \dots, N\}$ in Eqn. (5) runs over the valence states and the integer $N \geq N_v/2$ with N_v being the number of valence electrons. Furthermore, the linear transformation operator (\mathcal{T}) in Eqn. (5) is defined such that it differs from the Identity operator (\mathcal{I}) by a set of atom-specific transformations \mathcal{T}^a that has an effect only inside a certain atom-centered ball Ω_a with radius $|\mathbf{x} - \mathbf{R}_a| < r_c^a$ referred to as augmentation sphere. Consequently, the all-electron valence Kohn-Sham wavefunctions can be expressed as

$$\psi_i(\mathbf{x}) = \tilde{\psi}_i(\mathbf{x}) + \sum_a \sum_{\alpha} \left(\phi_{\alpha}^a(\mathbf{x}) - \tilde{\phi}_{\alpha}^a(\mathbf{x}) \right) \int_{\Omega_a} \tilde{p}_{\alpha}^a(\mathbf{y}) \tilde{\psi}_i(\mathbf{y}) d\mathbf{y} \quad (6)$$

where $\{\phi_{\alpha}^a\}$ are the all-electron partial waves, $\{\tilde{\phi}_{\alpha}^a\}$ are the pseudo-smooth partial waves that are used to expand $\{\psi_i(\mathbf{x})\}$ and $\{\tilde{\psi}_i(\mathbf{x})\}$ inside the augmentation sphere. Further, $\{\tilde{p}_{\alpha}^a\}$ in Eqn. (6) are the projector functions that are orthogonal to the pseudo smooth partial waves i.e., $\langle \tilde{p}_{\alpha}^a | \tilde{\phi}_{\beta}^a \rangle = \delta_{\alpha\beta}$. In the above Eqn. (6) and subsequently in the manuscript, the atom-centered fields are denoted with superscript 'a', implicitly denoting their functional dependence on $(\mathbf{x} - \mathbf{R}^a)$. Furthermore, the atom-centered functions $\{\tilde{p}_{\alpha}^a\}$, $\{\phi_{\alpha}^a\}$, $\{\tilde{\phi}_{\alpha}^a\}$ in Eqn. (6) are of the separable form $\vartheta_{\alpha}(r) S_{lm}(\hat{\theta})$, with $\vartheta_{\alpha}(r)$ being a radial function and $S_{lm}(\hat{\theta})$ is the real-spherical harmonic function that denotes the angular part of these atom-centered functions. We note that $r = |\mathbf{x} - \mathbf{R}^a|$ and $\hat{\theta} \in \mathbb{R}^2$ represents the azimuthal and polar components of $(\mathbf{x} - \mathbf{R}^a)$. Moreover, we note that the compact support of the functions $\tilde{p}_{\alpha}^a(\mathbf{x})$ and $(\phi_{\alpha}^a(\mathbf{x}) - \tilde{\phi}_{\alpha}^a(\mathbf{x}))$ lies in the augmentation sphere Ω_a , and consequently the decomposition in Eqn. (6) transforms the orthonormality requirement of all-electron Kohn-Sham wavefunctions to

\mathcal{S} -orthonormality ($\mathcal{S} = \mathcal{T}^\dagger \mathcal{T}$) condition on the pseudo-smooth(PS) wavefunctions $\{\tilde{\psi}_i\}$ i.e. $\langle \tilde{\psi}_i | \mathcal{S} | \tilde{\psi}_j \rangle = \delta_{ij}$. Eqn. (6), further allows the decomposition of the all-electron density $n(\mathbf{x})$ into a pseudo-smooth (PS) electron density $\tilde{n}(\mathbf{x})$ and an atom-centered correction which replaces the PS electron density inside the augmentation sphere with the true all-electron density and is given by

$$n(\mathbf{x}) = \tilde{n}(\mathbf{x}) + \sum_a (n^a(\mathbf{x}) - \tilde{n}^a(\mathbf{x})) \quad (7)$$

$$\text{with, } \tilde{n}(\mathbf{x}) = 2 \sum_i^N f_i |\tilde{\psi}_i(\mathbf{x})|^2 + \tilde{n}_c(\mathbf{x}) \quad (8)$$

$$\text{while, } n^a(\mathbf{x}) = n_c^a(\mathbf{x}) + \sum_{\alpha\beta} \phi_{\alpha}^a(\mathbf{x}) \phi_{\beta}^a(\mathbf{x}) D_{\alpha\beta}^a \quad (9)$$

$$\text{and } \tilde{n}^a(\mathbf{x}) = \tilde{n}_c^a(\mathbf{x}) + \sum_{\alpha\beta} \tilde{\phi}_{\alpha}^a(\mathbf{x}) \tilde{\phi}_{\beta}^a(\mathbf{x}) D_{\alpha\beta}^a \quad (10)$$

In the above equations, $n^a(\mathbf{x})$ represents the atom-centered all-electron density and $\tilde{n}^a(\mathbf{x})$, the atom-centered PS electron density that matches with $n^a(\mathbf{x})$ outside the augmentation sphere. Further, the matrix-components of the atom-dependent Hermitian matrix \mathbf{D}^a (often referred to as channel occupancy matrix [50] or spherical density matrix [52]) are given by

$$D_{\alpha\beta}^a = 2 \sum_i f_i \langle \tilde{\psi}_i | \tilde{p}_{\alpha}^a \rangle \langle \tilde{p}_{\beta}^a | \tilde{\psi}_i \rangle \quad (11)$$

Using the decompositions in Eqns. (6) and (7), the all-electron kinetic energy $T_s[\{\psi_i\}]$ and the exchange correlation energy $E_{\text{xc}}[n(\mathbf{x})]$ can be split into a smooth contribution and an atom-centered correction term as follows:

$$\begin{aligned} T_s[\{\psi_i\}] &= T_s[\{\tilde{\psi}_i\}] + \sum_a T_{\text{core}}^a + \sum_a \sum_{\alpha\beta} \Delta T_{\alpha\beta}^a D_{\alpha\beta}^a \\ E_{\text{xc}}[n(\mathbf{x})] &= E_{\text{xc}}[\tilde{n}(\mathbf{x})] + \sum_a \Delta E_{\text{xc}}^a \end{aligned} \quad (12)$$

where T_{core}^a is the kinetic energy contribution from the core states while the terms $\Delta T_{\alpha\beta}^a, \Delta E_{\text{xc}}^a$ are atomic corrections computed as

$$\begin{aligned} \Delta T_{\alpha\beta}^a &= -\frac{1}{2} \int_{\Omega_a} \left(\phi_{\alpha}^a(\mathbf{x}) \nabla^2 \phi_{\beta}^a(\mathbf{x}) - \tilde{\phi}_{\alpha}^a(\mathbf{x}) \nabla^2 \tilde{\phi}_{\beta}^a(\mathbf{x}) \right) d\mathbf{x} \\ \Delta E_{\text{xc}}^a &= \int_{\Omega_a} (\epsilon_{\text{xc}}[n^a, \nabla n^a] - \epsilon_{\text{xc}}[\tilde{n}^a, \nabla \tilde{n}^a]) d\mathbf{x} \end{aligned} \quad (13)$$

Finally, the all-electron electrostatics energy is decomposed into a smooth contribution and an atom-centered correction term by introducing a compensation charge $\tilde{b}^a(\mathbf{x})$ compactly supported in Ω_a so that the multipole moments of $(n^a(\mathbf{x}) - \tilde{n}^a(\mathbf{x}) + b^a(\mathbf{x}) - \tilde{b}^a(\mathbf{x}))$ vanish [11] inside Ω_a . To this end, the compensation charge $\tilde{b}^a(\mathbf{x})$ in terms of atom-centered spherical shape functions $\tilde{g}_{lm}^a(\mathbf{x})$ is given by

$$\tilde{b}^a(\mathbf{x}) = \kappa^a \tilde{g}_0^a(\mathbf{x}) + \sum_{lm, \alpha\beta} \Delta_{lm\alpha\beta}^a D_{\alpha\beta}^a \tilde{g}_{lm}^a(\mathbf{x}) \quad (14)$$

The atom-centered shape functions $\tilde{g}_{lm}^a(\mathbf{x})$ in the above Eqn. (14) are compactly supported in Ω_a and are usually constructed in the form of Gaussians, sinc-squared or Bessel functions [11, 50–52, 56] to satisfy the condition $\int_{\Omega_a} r^l S_{lm}(\hat{\boldsymbol{\theta}}) \tilde{g}_{lm'}^a(\mathbf{x}) d\mathbf{x} = \delta_{ll'} \delta_{mm'}$. Furthermore κ^a and $\Delta_{lm\alpha\beta}^a$ in Eqn. (14) are given by

$$\kappa^a = \int_{\Omega_a} (n_c^a(r) - \tilde{n}_c^a(r)) r^2 dr - z^a / \sqrt{4\pi}$$

$$\Delta_{lm\alpha\beta}^a = \int_{\Omega_a} r^l \left(\phi_\alpha^a(\mathbf{x}) \phi_\beta^a(\mathbf{x}) - \tilde{\phi}_\alpha^a(\mathbf{x}) \tilde{\phi}_\beta^a(\mathbf{x}) \right) S_{lm}(\hat{\boldsymbol{\theta}}) d\mathbf{x}$$

Now, the all-electron electrostatic energy can be computed as

$$J[\rho(\mathbf{x}), \{\mathbf{R}^a\}] = E_{\text{el}}[\tilde{\rho}(\mathbf{x}), \{\mathbf{R}^a\}] + \sum_a \Delta E_{\text{el}}^a \quad (15)$$

where the smooth total density is given by $\tilde{\rho}(\mathbf{x}) = \tilde{n}(\mathbf{x}) + \tilde{b}(\mathbf{x})$, with $\tilde{b}(\mathbf{x}) = \sum_a \tilde{b}^a(\mathbf{x})$. The electrostatic energy involving $\tilde{\rho}(\mathbf{x})$ is given by

$$E_{\text{el}}[\tilde{\rho}(\mathbf{x}), \{\mathbf{R}^a\}] = \frac{1}{2} \int \int \frac{\tilde{\rho}(\mathbf{x}) \tilde{\rho}(\mathbf{y})}{|\mathbf{x} - \mathbf{y}|} d\mathbf{x} d\mathbf{y} \quad (16)$$

and the atom-centered correction term is given by

$$\Delta E_{\text{el}}^a = E_{\text{el}}^a[\rho^a(\mathbf{r})] - E_{\text{el}}^a[\tilde{\rho}^a(\mathbf{r})] - E_{\text{self}}^a[\mathbf{R}^a] \quad \text{where}$$

$$E_{\text{el}}^a[\rho^a(\mathbf{r})] = \frac{1}{2} \int_{\Omega_a} \int_{\Omega_a} \frac{\rho^a(\mathbf{r}) \rho^a(\mathbf{r}')}{|\mathbf{r} - \mathbf{r}'|} d\mathbf{r} d\mathbf{r}'$$

$$E_{\text{el}}^a[\tilde{\rho}^a(\mathbf{r})] = \frac{1}{2} \int_{\Omega_a} \int_{\Omega_a} \frac{\tilde{\rho}^a(\mathbf{r}) \tilde{\rho}^a(\mathbf{r}')}{|\mathbf{r} - \mathbf{r}'|} d\mathbf{r} d\mathbf{r}' \quad (17)$$

with $\rho^a(\mathbf{x}) = n^a(\mathbf{x}) + b^a(\mathbf{x})$ and $\tilde{\rho}^a(\mathbf{x}) = \tilde{n}^a(\mathbf{x}) + \tilde{b}^a(\mathbf{x})$. The choice of the compensation charge in Eq. (14) allows one to evaluate ΔE_{el}^a only within the augmentation sphere Ω_a . Combining the various atom-centered correction terms from different energy contributions into ΔE^a , the all-electron energy in Eqn. (1) in PAW method is

reformulated as follows:

$$E[\{\psi_i\}, \{\mathbf{R}^a\}] = \tilde{E}[\{\tilde{\psi}_i\}, \{\mathbf{R}^a\}] + \sum_a \Delta E^a[\{D_{\alpha\beta}^a\}] \quad (18)$$

where we define $\tilde{E}[\{\tilde{\psi}_i\}, \{\mathbf{R}^a\}]$ and $\Delta E^a[\{D_{\alpha\beta}^a\}]$ as,

$$\tilde{E}[\{\tilde{\psi}_i\}, \{\mathbf{R}^a\}] = T_s[\{\tilde{\psi}_i\}] + E_{\text{xc}}[\tilde{n}(\mathbf{x})] + E_{\text{el}}[\tilde{\rho}(\mathbf{x}), \{\mathbf{R}^a\}]$$

$$\Delta E^a[\{D_{\alpha\beta}^a\}] = \Delta E_{\text{xc}}^a + \Delta E_{\text{el}}^a + \sum_{\alpha\beta} \Delta T_{\alpha\beta}^a D_{\alpha\beta}^a + T_{\text{core}}^a$$

At this juncture, from Eq.(18), we note that the all-electron Kohn-Sham energy functional of $\{\psi_i\}$ has been decomposed into a energy functional of smooth wavefunctions $\{\tilde{\psi}_i\}$ and a term that includes atomic corrections. The validity of this decomposition is reliant on two key assumptions. First, it is assumed that the augmentation spheres are non-overlapping and to achieve this, specialised PAW data sets are generated based on the application of interest [66]. Second assumption is that the set of partial waves ($\{\phi_\alpha\}$ and $\{\tilde{\phi}_\alpha\}$) forms a complete basis within the augmentation sphere. However, in practice, only a finite number of partial waves are used. The error arising from this incompleteness is mitigated by introducing an atom-specific zero potential $\tilde{v}^a(\mathbf{x})$ with a compact support only inside augmentation sphere [11, 50, 51].

The electrostatic interaction energy involving the smooth total density $E_{\text{el}}[\tilde{\rho}(\mathbf{x}), \{\mathbf{R}^a\}]$ in Eqn. (16) is extended in real-space and can be reformulated as a local variational problem in the spirit of [23, 67, 68]. Subsequently, the variational problem involved in computing this electrostatic energy contribution is given by:

$$E_{\text{el}}[\tilde{\rho}, \{\mathbf{R}^a\}] = -\max_{\varphi \in \gamma} \left\{ \frac{1}{8\pi} \int |\nabla \varphi(\mathbf{x})|^2 d\mathbf{x} - \int \tilde{\rho}(\mathbf{x}) \varphi(\mathbf{x}) d\mathbf{x} \right\} \quad (19)$$

where $\varphi(\mathbf{x}, \{\mathbf{R}^a\})$ denotes the trial function corresponding to electrostatic potential due to smooth electron-density (\tilde{n}) and the sum of atom-centered compensation charges ($\tilde{b}(\mathbf{x})$). Finally, the problem of determining the all-electron ground state energy and the all-electron density for a given position of nuclei is expressed as the following variational problem involving the smooth electronic fields:

$$E_{\text{GS}} = \min_{\{\tilde{\psi}_i\} \in \mathcal{X}} \max_{\varphi \in \gamma} \left\{ T_s[\{\tilde{\psi}_i\}] - \frac{1}{8\pi} \int |\nabla \varphi(\mathbf{x})|^2 d\mathbf{x} + \int \tilde{\rho}(\mathbf{x}) \varphi(\mathbf{x}) d\mathbf{x} + E_{\text{xc}}[\tilde{n}(\mathbf{x})] + \sum_a \Delta E^a[\{D_{\alpha\beta}^a\}] \right\} \quad (20)$$

where the function space $\mathcal{X} = \left\{ \{\tilde{\psi}_i\} \left| \left\langle \tilde{\psi}_p, \tilde{\psi}_q \right\rangle_{\mathbb{X}} = \delta_{pq} \right. \right\}$ with $\left\langle \tilde{\psi}_p, \tilde{\psi}_q \right\rangle$ denoting the \mathcal{S} -inner product $\langle \tilde{\psi}_p | \mathcal{S} | \tilde{\psi}_q \rangle$ defined on \mathbb{X} . The space \mathbb{X} denotes a suitable function

space that guarantees the existence of the minimisers. The domains used for numerical computations that are non-periodic corresponds to a large enough domain such that the wavefunctions $\{\tilde{\psi}_i\}$ decays to 0 and in periodic calculations, these correspond to supercells with periodic

boundary conditions. Denoting such an appropriate domain by Ω , the appropriate function spaces for \mathbb{X} and γ are $\mathbb{X} = \gamma = H_0^1(\Omega)$ in the case of non-periodic problems and $\mathbb{X} = \gamma = H_{\text{per}}^1(\Omega)$ in the case of periodic problems.

A. Governing Equations

The stationarity condition with respect to smooth fields $\{\psi_i\}$ corresponding to the PAW variational problem in Eqn. (20) gives rise to nonlinear generalized Hermitian eigenvalue problem (GHEP) of the following form:

$$\mathcal{H}\tilde{\psi}_i = \varepsilon_i \mathcal{S}\tilde{\psi}_i \quad (21)$$

where \mathcal{H} is a Hermitian operator with

$$\begin{aligned} \mathcal{H} &= -\frac{1}{2}\nabla^2 + V_{\text{eff}}(\tilde{\rho}, \{\mathbf{R}^a\}) + \mathcal{H}_{\text{nloc}} \\ \mathcal{H}_{\text{nloc}}\tilde{\psi}_i &:= \sum_a \sum_{\alpha\beta} \tilde{p}_\alpha^a(\mathbf{x}) \Delta h_{\alpha\beta}^a \int \tilde{p}_\beta^a(\mathbf{y}) \tilde{\psi}_i(\mathbf{y}) d\mathbf{y} \end{aligned} \quad (22)$$

and \mathcal{S} is a positive-definite Hermitian operator with

$$\begin{aligned} \mathcal{S} &= \mathcal{I} + \mathcal{S}_{\text{nloc}} \\ \mathcal{S}_{\text{nloc}}\tilde{\psi}_i &:= \sum_a \sum_{\alpha\beta} \tilde{p}_\alpha^a(\mathbf{x}) \Delta s_{\alpha\beta}^a \int \tilde{p}_\beta^a(\mathbf{y}) \tilde{\psi}_i(\mathbf{y}) d\mathbf{y} \end{aligned} \quad (23)$$

The set $(\{\varepsilon_i\}, \{\tilde{\psi}_i\})$ are the eigenvalue and eigenfunction pairs of the generalised eigenvalue problem (21) and the N smallest eigenvalue and eigenvector pairs are used to compute the PS density $\tilde{n}(\mathbf{x})$ and the matrix \mathbf{D}^a employing the Eqns. (8) and Eq. (11) respectively. Further, the effective potential (V_{eff}) comprising of the total electrostatic potential, exchange-correlation potential and zero potential is computed as

$$V_{\text{eff}} = V_{\text{el}} + V_{\text{xc}} + \bar{V} = \frac{\delta E_{\text{el}}}{\delta \tilde{n}} + \frac{\delta E_{\text{xc}}}{\delta \tilde{n}} + \sum_a \bar{v}^a \quad (24)$$

where the electrostatic potential $\frac{\delta E_{\text{el}}}{\delta \tilde{n}} = \varphi(\mathbf{x}, \{\mathbf{R}^a\})$ is computed as the solution of the Poisson equation associated with the smooth total density $\tilde{\rho}(\mathbf{x})$ as given by eq.(19). Furthermore, the atom centered contributions

$\Delta h_{\alpha\beta}^a$ and $\Delta s_{\alpha\beta}^a$ in $\mathcal{H}_{\text{nloc}}$ and $\mathcal{S}_{\text{nloc}}$ are expressed as

$$\begin{aligned} \Delta h_{\alpha\beta}^a &= \frac{\delta \Delta E^a}{\delta D_{\alpha\beta}^a} + \sum_{lm} \Delta_{lm\alpha\beta}^a \int_{\Omega_a} \tilde{g}_{lm}^a(\mathbf{x}) \varphi(\mathbf{x}) d\mathbf{x} \\ &\quad - \int_{\Omega_a} \bar{v}^a(\mathbf{x}) \tilde{\phi}_\alpha^a(\mathbf{x}) \tilde{\phi}_\beta^a(\mathbf{x}) d\mathbf{x} \end{aligned} \quad (25)$$

$$\Delta s_{\alpha\beta}^a = \int_{\Omega_a} \left(\phi_\alpha^a(\mathbf{x}) \phi_\beta^a(\mathbf{x}) - \tilde{\phi}_\alpha^a(\mathbf{x}) \tilde{\phi}_\beta^a(\mathbf{x}) \right) d\mathbf{x} = \sqrt{4\pi} \Delta_{00\alpha\beta}^a \quad (26)$$

Finally, the set of governing differential equations to be solved in the PAW method are:

$$\begin{aligned} \left(-\frac{1}{2}\nabla^2 + V_{\text{eff}}(\tilde{\rho}, \{\mathbf{R}^a\}) + \mathcal{H}_{\text{nloc}} \right) \tilde{\psi}_i &= \varepsilon_i (\mathcal{I} + \mathcal{S}_{\text{nloc}}) \tilde{\psi}_i \\ 2 \sum_i f(\varepsilon_i, \mu) &= N_v, \quad f(\varepsilon_i, \mu) = \frac{1}{1 + \exp\left(\frac{\varepsilon_i - \mu}{\sigma}\right)} \\ \tilde{n}(\mathbf{x}) &= 2 \sum_i f(\varepsilon_i, \mu) |\tilde{\psi}_i(\mathbf{x})|^2, \quad \tilde{b}(\mathbf{x}) = \sum_a \tilde{b}^a(\mathbf{x}) \\ \tilde{b}^a(\mathbf{x}) &= \kappa^a \tilde{g}_0^a(\mathbf{x}) + \sum_{lm, \alpha\beta} \Delta_{lm\alpha\beta}^a D_{\alpha\beta}^a \tilde{g}_{lm}^a(\mathbf{x}) \\ \hat{U}_{\alpha i}^a &= \int \tilde{p}_\alpha^a(\mathbf{y}) \tilde{\psi}_i(\mathbf{y}) d\mathbf{y}, \quad D_{\alpha\beta}^a = 2 \sum_i f(\varepsilon_i, \mu) \hat{U}_{\alpha i}^{a*} \hat{U}_{i\beta}^a \\ \tilde{\rho}(\mathbf{x}) &= \tilde{n}(\mathbf{x}) + \tilde{b}(\mathbf{x}), \quad -\frac{1}{4\pi} \nabla^2 \varphi(\mathbf{x}, \{\mathbf{R}^a\}) = \tilde{\rho}(\mathbf{x}) \end{aligned} \quad (27)$$

where $\hat{u}_{\alpha i}^{a*}$ is the complex conjugate of $\hat{u}_{\alpha i}^a$, μ is the Fermi energy and $f_i := f(\varepsilon_i, \mu)$ is the orbital occupancy function lying in the interval $[0, 1]$ which is computed -via- the Fermi-Dirac distribution with $\sigma = k_B T$ where T is the smearing temperature and k_B is the Boltzmann constant.

When dealing with periodic crystals, 2D periodic slabs, or surfaces, it is computationally efficient to invoke the Bloch theorem[64, 69] along the periodic axes. Here, instead of solving the DFT problem on a large periodic supercell, we solve the reduced problem on a smaller unit-cells with periodic boundary conditions. By invoking Bloch theorem, the eigenfunctions of the PAW generalised eigenvalue problem can be expressed as

$$\tilde{\psi}_{i,\mathbf{k}}(\mathbf{x}) = e^{i\mathbf{k} \cdot \mathbf{x}} \tilde{u}_{i,\mathbf{k}}(\mathbf{x}) \quad (28)$$

where $i = \sqrt{-1}$ and $\tilde{u}_{i,\mathbf{k}}(\mathbf{x})$ is a unit-cell periodic complex valued function satisfying $\tilde{u}_{i,\mathbf{k}}(\mathbf{x} + \mathbf{L}_r) = \tilde{u}_{i,\mathbf{k}}(\mathbf{x})$ for all lattice vectors \mathbf{L}_r with \mathbf{k} denoting a point in the first Brillouin zone(BZ) of the reciprocal lattice. The set of governing equations for the PAW formalism with Bloch wavefunctions $\tilde{u}_{i,\mathbf{k}}(\mathbf{x})$ can be recast as:

$$\begin{aligned}
& \left(-\frac{1}{2}\nabla^2 - \mathbf{i}\mathbf{k} \cdot \nabla + \frac{1}{2}|\mathbf{k}|^2 + V_{\text{eff}}(\tilde{\rho}, \{\mathbf{R}^a\}) + \mathcal{H}_{\text{nloc}}^{\mathbf{k}} \right) \tilde{u}_{i,\mathbf{k}} = \varepsilon_{i,\mathbf{k}} (\mathcal{I} + \mathcal{S}_{\text{nloc}}^{\mathbf{k}}) \tilde{u}_{i,\mathbf{k}} \text{ on } \Omega_p, \quad \forall \mathbf{k} \in BZ \\
& \mathcal{H}_{\text{nloc}}^{\mathbf{k}} \tilde{u}_{i,\mathbf{k}} := \sum_a \sum_{\alpha\beta} \sum_r e^{-i\mathbf{k} \cdot (\mathbf{x} - \mathbf{L}_r)} \tilde{p}_\alpha^a(\mathbf{x} - (\mathbf{R}^a + \mathbf{L}_r)) \Delta h_{\alpha\beta}^a U_{\beta i}^{a\mathbf{k}}, \\
& \mathcal{S}_{\text{nloc}}^{\mathbf{k}} \tilde{u}_{i,\mathbf{k}} := \sum_a \sum_{\alpha\beta} \sum_r e^{-i\mathbf{k} \cdot (\mathbf{x} - \mathbf{L}_r)} \tilde{p}_\alpha^a(\mathbf{x} - (\mathbf{R}^a + \mathbf{L}_r)) \Delta s_{\alpha\beta}^a U_{\beta i}^{a\mathbf{k}} \\
& 2 \sum_i \oint_{BZ} 2f(\varepsilon_{i,\mathbf{k}}, \mu) d\mathbf{k} = N_v, \quad f(\varepsilon_{i,\mathbf{k}}, \mu) = \frac{1}{1 + \exp\left(\frac{\varepsilon_{i,\mathbf{k}} - \mu}{\sigma}\right)}, \quad \tilde{n}(\mathbf{x}) = \sum_i \oint_{BZ} 2f(\varepsilon_{i,\mathbf{k}}, \mu) |\tilde{u}_{i,\mathbf{k}}(\mathbf{x})|^2 d\mathbf{k}, \quad \tilde{b}(\mathbf{x}) = \sum_a \tilde{b}^a(\mathbf{x}) \\
& \hat{U}_{\alpha i}^{a,\mathbf{k}} := \int_{\Omega_p} \sum_{r'} e^{i\mathbf{k} \cdot (\mathbf{y} - \mathbf{L}_{r'})} p_\alpha^a(\mathbf{y} - (\mathbf{R}^a + \mathbf{L}_{r'})) \tilde{u}_{i,\mathbf{k}}(\mathbf{y}) d\mathbf{y}, \quad D_{\alpha\beta}^a = 2 \sum_i \oint_{BZ} f(\varepsilon_i^{\mathbf{k}}, \mu) \hat{U}_{\alpha i}^{a,\mathbf{k}*} \hat{U}_{i\beta}^{a,\mathbf{k}} d\mathbf{k} \\
& \tilde{b}^a(\mathbf{x}) = \kappa^a \tilde{g}_0^a(\mathbf{x}) + \sum_{lm,\alpha\beta} \Delta_{lm\alpha\beta}^a D_{\alpha\beta}^a \tilde{g}_{lm}^a(\mathbf{x}), \quad \tilde{\rho}(\mathbf{x}) = \tilde{n}(\mathbf{x}) + \tilde{b}(\mathbf{x}), \quad -\frac{1}{4\pi} \nabla^2 \varphi(\mathbf{x}, \{\mathbf{R}^a\}) = \tilde{\rho}(\mathbf{x}) \quad (29)
\end{aligned}$$

where \oint_{BZ} denotes the volume average of the integral over the first Brillouin zone (BZ) corresponding to the periodic unit cell Ω_p . We further note that the equations corresponding to non-periodic case in Eqn.(27) can be easily recovered from the above equations (II A) by considering $(\mathbf{k} = 0, \mathbf{L}_r = 0)$ and replacing the periodic unit-cell domain Ω_p with a non-periodic simulation domain Ω . We note that semi-periodic boundary conditions can be handled in a similar way depending on the number of periodic directions. Furthermore, we note that the set of equations in Eqn.(27) or Eqn.(II A) involves a nonlinear generalized Hermitian eigenvalue problem (GHEP) that needs to be solved self-consistently in conjunction with the Poisson equation. In particular, we seek to solve the fixed point iteration corresponding to the total charge density $\tilde{\rho}(\mathbf{x}) = F(\tilde{\rho}(\mathbf{x}))$ using a self-consistent field (SCF) iteration procedure where the evaluation of the map $F(\tilde{\rho}(\mathbf{x}))$ involves the solution of the GHEP and the Poisson equation in Eqn.(II A) or Eqn.(27) at every SCF iteration.

III. PAW-FE: FINITE ELEMENT DISCRETIZATION FOR PAW METHOD

Finite-element method involves decomposing the spatial domain of interest into non-overlapping subdomains called finite-elements (or cells) using a finite-element (FE) mesh. The underlying FE basis functions spanning a finite-element subspace are piecewise polynomials that exhibit systematically convergent behaviour [70–72]. Furthermore, these basis functions are strictly local, having a compact support only in the finite-element cells sharing a finite-element node, making them well-suited for massive parallelization. In contrast to conventional finite-element basis typically constructed from a tensor product of Lagrange polynomials interpolated through equidistant nodal points in a given finite-element, in this

work, we specifically employ spectral finite-element basis that are C^0 continuous Lagrange polynomials generated using Gauss-Lobatto-Legendre (GLL) nodal points that are the roots of derivatives of Legendre polynomials. We refer to previous works [23, 27, 29, 42] about the advantages provided by higher-order adaptive spectral finite-element-based methods to solve the Kohn-Sham DFT problem in the context of norm-conserving pseudopotentials and all-electron DFT calculations. A crucial aspect of the computational methodology described below involves the use of these higher-order spectral finite-elements in conjunction with the reduced order Gauss-Lobatto Legendre (GLL) quadrature rules combined with the non-overlapping nature of augmentation spheres that enables the efficient inversion of the PAW overlap matrix. We discuss here the finite-element discretization of the governing equations deducing the algebraic generalized eigenvalue problem to be solved in the PAW method.

As seen from Eq.(20), the real-space formulation of the PAW method presented in this work results in a min-max problem involving the smooth pseudo-wavefunctions (\tilde{u} or φ) and the electrostatic potential. Employing a single FE discretization for both the wavefunctions and the electrostatic potential can result in non-variational behaviour of the electronic ground-state energy. Therefore, we seek a solution for the electrostatics problem -via- the Poisson equation with a more stringent accuracy than the eigenvalue problem solution employing different orders of FE interpolating polynomial basis for the electrostatic potential and the wavefunctions. To this end, we represent the electronic fields in Eq.(II A) in the FE basis and are given by

$$\tilde{u}_{i,\mathbf{k}}^h(\mathbf{x}) = \sum_{J=1}^M N_J^{h,p}(\mathbf{x}) \tilde{u}_{i,\mathbf{k}}^J, \quad \varphi^{h,p\text{el}}(\mathbf{x}) = \sum_{J=1}^{M_{\text{el}}} N_J^{h,p\text{el}}(\mathbf{x}) \varphi^J \quad (30)$$

where $\tilde{u}_{i,\mathbf{k}}^J, \varphi^J$ denote the FE discretized fields, while

$N_J^{h,p} : 1 \leq J \leq M$ and $N_J^{h,p_{el}} : 1 \leq J \leq M_{el}$ denote the strictly local Lagrange polynomial basis functions of degree p and p_{el} , respectively spanning the finite-element subspace, generated using the nodes of the FE triangulation \mathcal{T}^h with the characteristic mesh size denoted by h and $p_{el} > p$ as discussed. To this end, the finite-element discretization of the Kohn-Sham generalized eigenvalue problem in Eq.(II A) results in an algebraic generalized Hermitian eigenvalue problem $\mathbf{H}^{\mathbf{k}} \tilde{\mathbf{u}}_{i,\mathbf{k}} = \varepsilon_{i,\mathbf{k}}^h \mathbf{S}^{\mathbf{k}} \tilde{\mathbf{u}}_{i,\mathbf{k}}$, where $\mathbf{H}^{\mathbf{k}}$ and $\mathbf{S}^{\mathbf{k}}$ denote the discretized Hamiltonian matrix and the PAW overlap matrices of size $M \times M$ with $\varepsilon_{i,\mathbf{k}}^h$ denoting the i^{th} eigenvalue corresponding to the discrete eigenvector $\tilde{\mathbf{u}}_{i,\mathbf{k}}$. The finite-element discretized Hamiltonian and PAW overlap matrices has both local and non-local contributions and hence can be decomposed as $\mathbf{H}^{\mathbf{k}} = \mathbf{H}^{\mathbf{k},\text{loc}} + \mathbf{H}^{\mathbf{k},\text{nloc}}$ and $\mathbf{S}^{\mathbf{k}} = \mathbf{M} + \mathbf{S}^{\mathbf{k},\text{nloc}}$ where the matrix entries of the local contributions $\mathbf{H}^{\mathbf{k},\text{loc}}$ and \mathbf{M} are given by

$$\begin{aligned} \mathbf{H}_{IJ}^{\mathbf{k},\text{loc}} = & \int_{\Omega_p} \left\{ \frac{1}{2} \nabla N_I^{h,p}(\mathbf{x}) \cdot \nabla N_J^{h,p}(\mathbf{x}) \right. \\ & + V_{\text{eff}}^h(\mathbf{x}) N_I^{h,p}(\mathbf{x}) N_J^{h,p}(\mathbf{x}) \\ & + \frac{1}{2} |\mathbf{k}|^2 N_I^{h,p}(\mathbf{x}) N_J^{h,p}(\mathbf{x}) - i\mathbf{k} \cdot N_I^{h,p}(\mathbf{x}) \nabla N_J^{h,p}(\mathbf{x}) \\ & \left. + \mathbf{V}_{\text{GGA}}^h(\mathbf{x}) \cdot \left(N_I^{h,p}(\mathbf{x}) \nabla N_J^{h,p}(\mathbf{x}) + N_J^{h,p}(\mathbf{x}) \nabla N_I^{h,p}(\mathbf{x}) \right) \right\} d\mathbf{x} \end{aligned} \quad (31)$$

$$\mathbf{M}_{IJ} = \int_{\Omega_p} N_I^{h,p}(\mathbf{x}) N_J^{h,p}(\mathbf{x}) d\mathbf{x} \quad (32)$$

with

$$\begin{aligned} V_{\text{eff}}^h &= \left(\varphi^{h,p_{el}}(\mathbf{x}) + \bar{V}(\mathbf{x}) + \frac{\partial \epsilon_{\text{xc}}(\tilde{n}, \nabla \tilde{n})}{\partial \tilde{n}} \bigg|_{\tilde{n}=\tilde{n}^h} \right) \\ \mathbf{V}_{\text{GGA}}^h(\mathbf{x}) &= \frac{\partial \epsilon_{\text{xc}}(\tilde{n}, \nabla \tilde{n})}{\partial \nabla \tilde{n}} \bigg|_{\tilde{n}=\tilde{n}^h} \end{aligned}$$

and the discrete electrostatic potential $\varphi^{h,p_{el}}(\mathbf{x})$ in V_{eff}^h above is computed by taking recourse to the solution of the finite-element discretized Poisson equation $\mathbf{L}\Phi = \mathbf{c}$ where \mathbf{L} denotes the Laplace operator discretized using the finite-element basis $N_J^{h,p_{el}} : 1 \leq J \leq M_{el}$ while Φ denotes the electrostatic potential vector whose entries are the expansion coefficients φ^J in Eqn.(30) and \mathbf{c} denotes the forcing vector corresponding to $\tilde{\rho}$, the right-hand side of the Poisson equation in Eqn.(II A). To this end, the entries of \mathbf{L} and \mathbf{c} are given by

$$L_{IJ} = \frac{1}{4\pi} \int_{\Omega_p} \nabla N_I^{h,p_{el}}(\mathbf{x}) \cdot \nabla N_J^{h,p_{el}}(\mathbf{x}) d\mathbf{x}, \quad (33)$$

$$c_I = \int_{\Omega_p} \tilde{\rho}^h(\mathbf{x}) N_I^{h,p_{el}}(\mathbf{x}) d\mathbf{x} \quad (34)$$

Finally, the matrix entries corresponding to the non-local

contributions in $\mathbf{H}^{\mathbf{k}}$ and $\mathbf{S}^{\mathbf{k}}$ are given by

$$\begin{aligned} \mathbf{H}^{\mathbf{k},\text{nloc}} &= \sum_a \mathbf{C}^{a,\mathbf{k}} \Delta_{\mathbf{H}}^a \mathbf{C}^{a,\mathbf{k}\dagger}, \quad \mathbf{S}^{\mathbf{k},\text{nloc}} = \sum_a \mathbf{C}^{a,\mathbf{k}} \Delta_{\mathbf{S}}^a \mathbf{C}^{a,\mathbf{k}\dagger} \\ C_{J\alpha}^{a,\mathbf{k}} &= \int_{\Omega_p} \sum_r e^{-i\mathbf{k} \cdot (\mathbf{x} - \mathbf{L}_r)} \tilde{p}_{\alpha}^a(\mathbf{x} - (\mathbf{R}^a + \mathbf{L}_r)) N_J^{h,p}(\mathbf{x}) d\mathbf{x} \end{aligned}$$

where the atom-dependent coupling matrices $\Delta_{\mathbf{H}}^a$ and $\Delta_{\mathbf{S}}^a$ are of size $n_{\text{pj}}^a \times n_{\text{pj}}^a$ with n_{pj}^a denoting the number of projectors for atom index a and the corresponding matrix entries denoted as $\Delta h_{\alpha\beta}^{a,h}$ and $\Delta s_{\alpha\beta}^a$ respectively are given by

$$\begin{aligned} \Delta h_{\alpha\beta}^{a,h} &= \frac{\delta \Delta E^{a,h}}{\delta D_{\alpha\beta}^a} + \sum_{lm} \Delta_{lm\alpha\beta}^a \int_{\Omega_a} \tilde{g}_{lm}^a(\mathbf{x}) \varphi^{h_{el}}(\mathbf{x}) d\mathbf{x} \\ &- \int_{\Omega_a} \bar{v}^a(\mathbf{x}) \tilde{\phi}_{\alpha}^a(\mathbf{x}) \tilde{\phi}_{\beta}^a(\mathbf{x}) d\mathbf{x}; \quad \Delta s_{\alpha\beta}^a = \sqrt{4\pi} \Delta_{00\alpha\beta}^a \end{aligned} \quad (35)$$

We note that the matrices $\mathbf{H}^{\mathbf{k},\text{loc}}$ and $\mathbf{S}^{\mathbf{k},\text{loc}}$ are sparse as the finite-element (FE) basis functions are localized in real-space. Since the projectors $\tilde{p}^a(\mathbf{x} - \mathbf{R}^a)$ have a compact support within the augmentation sphere Ω_a , we note that the $M \times n_{\text{pj}}^a$ matrix $\mathbf{C}^{a,\mathbf{k}}$ is also a sparse matrix for every atom a . Consequently, we can now rewrite the discretized Hamiltonian matrix and the overlap matrix within the PAW formalism as

$$\mathbf{H}^{\mathbf{k}} = \mathbf{H}_{\text{loc}}^{\mathbf{k}} + \mathbf{P}^{\mathbf{k}} \Delta_{\mathbf{H}} \mathbf{P}^{\mathbf{k}\dagger}, \quad \mathbf{S}^{\mathbf{k}} = \mathbf{M} + \mathbf{P}^{\mathbf{k}} \Delta_{\mathbf{S}} \mathbf{P}^{\mathbf{k}\dagger} \quad (36)$$

where the $M \times n_{\text{proj}}$ matrix $\mathbf{P}^{\mathbf{k}} = [\mathbf{C}^{1,\mathbf{k}} \dots \mathbf{C}^{a,\mathbf{k}} \dots \mathbf{C}^{N_a,\mathbf{k}}]$, with $n_{\text{proj}} = \sum_a n_{\text{pj}}^a$ denoting the total number of atomic projectors in the system. In the above Eqn.(36), $\Delta_{\mathbf{H}}$ and $\Delta_{\mathbf{S}}$ are the block diagonal matrices of size $n_{\text{proj}} \times n_{\text{proj}}$ with each block corresponding to the atom-dependent coupling matrices $\Delta_{\mathbf{H}}^a$ and $\Delta_{\mathbf{S}}^a$ respectively as introduced in Eqn.(35).

Finally, the discretized governing equations corresponding to Eqn. (II A) that need to be solved in PAW-FE are given by:

$$\begin{aligned} \mathbf{H}^{\mathbf{k}} \tilde{\mathbf{u}}_{i,\mathbf{k}} &= \varepsilon_{i,\mathbf{k}}^h \mathbf{S}^{\mathbf{k}} \tilde{\mathbf{u}}_{i,\mathbf{k}} \\ 2 \sum_n \int_{BZ} f(\varepsilon_{i,\mathbf{k}}^h, \mu) d\mathbf{k} &= N_v, \quad f(\varepsilon_{i,\mathbf{k}}^h, \mu) = \frac{1}{1 + \exp\left(\frac{\varepsilon_{i,\mathbf{k}}^h - \mu}{\sigma}\right)} \\ \tilde{n}^h(\mathbf{x}) &= 2 \sum_i \int_{BZ} f(\varepsilon_{i,\mathbf{k}}^h, \mu) |\tilde{u}_{i,\mathbf{k}}^h(\mathbf{x})|^2 d\mathbf{k}, \quad \hat{\mathbf{U}}_i^{a,\mathbf{k}} = \mathbf{C}^{a,\mathbf{k}\dagger} \tilde{\mathbf{u}}_{i,\mathbf{k}} \\ D_{\alpha\beta}^{a,h} &= 2 \sum_i \int_{BZ} f(\varepsilon_{i,\mathbf{k}}^h, \mu) \hat{U}_{\alpha i}^{a,\mathbf{k}*} \hat{U}_{\beta i}^{a,\mathbf{k}} d\mathbf{k} \\ \tilde{b}^h(\mathbf{x}) &= \sum_a \tilde{b}^{a,h}(\mathbf{x}), \quad \tilde{\rho}^h(\mathbf{x}) = \tilde{n}^h(\mathbf{x}) + \tilde{b}^h(\mathbf{x}), \quad \mathbf{L}\Phi = \mathbf{c} \end{aligned} \quad (37)$$

We note that the discretized generalized Hermitian eigenvalue problem (GHEP) in the above Eqn.(37) is

a nonlinear eigenproblem and is solved for N smallest eigenvalue-eigenvector pairs, which in turn are used to evaluate the smooth pseudo density $\tilde{n}^h(\mathbf{x})$ and the atom-centred density matrix $\{D_{\alpha\beta}^{a,h}\}$. This nonlinear GHEP is self-consistently solved in conjunction with the discretized Poisson equation subject to the applied boundary conditions in order to obtain the ground-state electronic fields and the energy. As noted before, replacing the periodic unit-cell domain Ω_p with a non-periodic simulation domain Ω and considering $\mathbf{k} = 0$, $\mathbf{L}_r = 0$, we recover the finite-element discretized equations corresponding to non-periodic boundary conditions from Eqn.(37). Subsequently, the total all-electron energy in the PAW method, \tilde{E}^h in terms of the finite-element discretized ground-state solution fields $(\varepsilon_{n,\mathbf{k}}^h, \tilde{n}^h(\mathbf{x}), D_{\alpha\beta}^{a,h}, \varphi^{h,p_{el}})$ is given by

$$\begin{aligned} \tilde{E}^h = & 2 \sum_{i=1}^N \oint_{BZ} f(\varepsilon_{i,\mathbf{k}}^h, \mu) \varepsilon_{i,\mathbf{k}}^h d\mathbf{k} - \sum_a \sum_{ij} \Delta h_{\alpha\beta}^a D_{\alpha\beta}^{a,h} \\ & - \int_{\Omega_p} [\tilde{n}^h(\mathbf{x}) V_{\text{eff}}^h(\mathbf{x}) + \mathbf{V}_{\text{eff,GGA}}^h(\mathbf{x}) \cdot \nabla \tilde{n}^h(\mathbf{x})] d\mathbf{x} \\ & + \frac{1}{2} \int_{\Omega_p} \tilde{\rho}^h(\mathbf{x}) \varphi^{h,p_{el}}(\mathbf{x}) d\mathbf{x} + E_{\text{xc}}[\tilde{n}^h(\mathbf{x})] \\ & + \sum_a \Delta E^a [\{D_{\alpha\beta}^{a,h}\}] \end{aligned} \quad (38)$$

The various computational aspects involved in efficiently solving the nonlinear generalized eigenvalue problem (Eqn. (37)) using a self-consistent field (SCF) iteration procedure are discussed in the subsequent section. In the following section, we choose to drop the \mathbf{k} index in the FE discretized electronic fields, vectors and matrices introduced in Eqn. (36) for brevity, and we refer to them as $\tilde{u}_i^h(\mathbf{x})$, $\tilde{\mathbf{u}}_i$, \mathbf{H} , \mathbf{S} and \mathbf{P} without the \mathbf{k} index.

IV. SELF CONSISTENT FIELD ITERATION

In this section, we begin by describing the self-consistent field iteration (SCF) procedure adopted in our work to solve the nonlinear PAW generalized eigenvalue problem, highlighting the real-space mixing strategy employed in our work suited towards solving the Kohn-Sham fixed point problem inherent in the PAW method. Subsequently, we describe the Chebyshev filtering subspace iteration (ChFSI) approach and the related modifications to adapt ChFSI for efficiently solving the underlying generalized eigenvalue problem within a given SCF iteration. Additionally, we elaborate on the key computational strategies that leverage the underlying sparse finite-element structure and the compact support of the PAW projectors in real-space to facilitate fast and scalable calculations of computationally intensive steps in the ChFSI approach.

The finite-element discretized governing equations (37) in the PAW method involves the solution of a nonlinear

Algorithm 1: Self-consistent field iteration

Output: Self consistently converged total charge

density $\tilde{\rho}^h(\mathbf{x}) = \tilde{n}^h(\mathbf{x}) + \tilde{b}^h(\mathbf{x})$

1. Provide initial guess for $\tilde{n}_0^h(\mathbf{x})$ and $\{\mathbf{D}_0^{a,h}\}$ from PAW dataset. The initial guess will be used as the input for the first SCF iteration ($\tilde{n}_{\text{in}}^h(\mathbf{x}) = \tilde{n}_0^h(\mathbf{x}), \{\mathbf{D}_{\text{in}}^{a,h}\} = \{\mathbf{D}_0^{a,h}\}$).
 2. Compute the total electrostatic potential $\varphi^{h,p_{el}}(\mathbf{x})$ for the charge density $(\tilde{n}^h(\mathbf{x}) + \tilde{b}^h(\mathbf{x}))$ by solving the discrete Poisson equation.
 3. Compute the effective potential $(\mathbf{V}_{\text{eff,GGA}}^h(\mathbf{x}), V_{\text{eff}}^h(\mathbf{x}))$ and Hamiltonian coupling matrix $(\Delta_{\mathbf{H}}^a)$ used to compute the Hamiltonian (\mathbf{H}) .
 4. Solve the linearized PAW generalised eigenvalue problem $\mathbf{H}\tilde{\mathbf{u}}_i = \varepsilon_i \mathbf{S}\tilde{\mathbf{u}}_i$ to obtain the eigenfunctions $\tilde{u}_{i,\mathbf{k}}^h(\mathbf{x})$.
 5. Compute the new output electron density $\tilde{n}_{\text{out}}^h(\mathbf{x})$ and $\{\mathbf{D}_{\text{out}}^{a,h}\}$ from the fractional occupancy $(f(\varepsilon_{i,\mathbf{k}}, \mu))$ and eigenfunctions $\tilde{u}_{i,\mathbf{k}}^h(\mathbf{x})$.
 6. If $||\tilde{\rho}_{\text{out}}^h(\mathbf{x}) - \tilde{\rho}_{\text{in}}^h(\mathbf{x})|| < \text{tol}$, stop; else, compute the new $\tilde{n}_{\text{in}}^h(\mathbf{x}), \{\mathbf{D}_{\text{in}}^{a,h}\}$ using Anderson[73] mixing scheme and go to step 2.
-

generalized eigenvalue problem that needs to be solved self-consistently as alluded to before. Since the total charge density is the sum of the smooth pseudo density (\tilde{n}) and the compensation charge (\tilde{b}) which is a function of the spherical density matrix \mathbf{D}^a , we note that the Kohn-Sham fixed point iteration map in the PAW method is written in terms of total charge density i.e $\tilde{\rho}_{\text{out}}^h(\mathbf{x}) = F(\tilde{\rho}_{\text{in}}^h(\mathbf{x}))$. To this end, we start with an input guess for the total charge density $\tilde{\rho}_{\text{in}} = \tilde{n}_{\text{in}}^h + \tilde{b}^h(\mathbf{D}_{\text{in}}^a)$ and the map $F(\tilde{\rho}_{\text{in}}^h(\mathbf{x}))$ involves evaluating the effective potential $(V_{\text{eff}}^h(\mathbf{x}), \mathbf{V}_{\text{GGA}}^h(\mathbf{x}))$, the non-local Hamiltonian coupling matrix $(\Delta_{\mathbf{H}}^a)$ using $\tilde{\rho}_{\text{in}}^h$ to compute the eigenpairs $(\varepsilon_i^h, \tilde{\mathbf{u}}_i)$ of the PAW generalized eigenvalue problem which are in turn used to output total charge density $\tilde{\rho}_{\text{out}} = \tilde{n}_{\text{out}}^h + \tilde{b}^h(\mathbf{D}_{\text{out}}^a)$. The above procedure is summarised in steps 2-5 of the Algorithm(1) that describes the SCF iteration and these steps are continued until $||\tilde{\rho}_{\text{out}}^h(\mathbf{x}) - \tilde{\rho}_{\text{in}}^h(\mathbf{x})||$ is lesser than the required tolerance, where $||\cdot||$ is some appropriate norm.

The computationally intensive step involved in the SCF iteration is solving the discretized generalised eigenvalue problem (step-4). This step asymptotically scales cubically with the system size, making it crucial to employ efficient numerical strategies to delay the onset of cubic scaling and reduce the number of SCF iterations. The following subsection describes the mixing strategy employed in our work to accelerate the convergence of SCF iteration

A. Total charge density mixing

In contrast to DFT calculations involving norm-conserving pseudopotentials and all-electron methods, where pseudo-valence electron density or the all-electron density is mixed during the SCF iteration, in the PAW method, the total charge density ($\tilde{\rho}(\mathbf{x}) = \tilde{n}(\mathbf{x}) + \tilde{b}(\mathbf{x})$) needs to be updated self consistently. This is because the compensation charge $\tilde{b}(\mathbf{x})$ depends on $\{\mathbf{D}^a\}$ which in turn depends on pseudo-smooth wavefunctions (see Eq.(14)) and hence needs to be mixed at every SCF iteration.

We employ a n -stage Anderson [73] mixing scheme to accelerate the SCF iteration in the current work, with appropriate modifications relevant to the real-space PAW framework as discussed in this section. Denoting input total charge densities and output total charge densities at the n^{th} SCF iteration as $\tilde{\rho}_{\text{in}}^{(n)}(\mathbf{x})$ and $\tilde{\rho}_{\text{out}}^{(n)}(\mathbf{x})$ respectively, the input total charge density for $(n+1)^{\text{th}}$ SCF iteration $\tilde{\rho}_{\text{in}}^{(n+1)}(\mathbf{x})$ is computed as

$$\tilde{\rho}_{\text{in}}^{(n+1)} = \gamma_{\text{mix}} \tilde{\rho}_{\text{out}} + (1 - \gamma_{\text{mix}}) \tilde{\rho}_{\text{in}} \quad (39)$$

where $\tilde{\rho}_{\text{in(out)}}$ is expressed as a linear combination of input and output total charge densities from n previous SCF iterations. To this end, we have

$$\tilde{\rho}_{\text{in(out)}} = \tilde{\rho}_{\text{in(out)}}^n + \sum_{k=1}^{n-1} c_k (\tilde{\rho}_{\text{in(out)}}^{(n-k)} - \tilde{\rho}_{\text{in(out)}}^{(n)}) \quad (40)$$

where we determine the linear combination coefficients c_k by minimizing the norm square of the residual $R = \|\tilde{\rho}_{\text{res}}\|_W^2 = \|\tilde{\rho}_{\text{out}}(\mathbf{x}) - \tilde{\rho}_{\text{in}}(\mathbf{x})\|_W^2$ with the weighted norm defined as

$$\|\tilde{\rho}_{\text{res}}\|_W^2 := \langle \tilde{\rho}_{\text{res}} | \mathcal{I} + \kappa_c | \tilde{\rho}_{\text{res}} \rangle \quad (41)$$

where κ_c in \mathbf{x} basis is the Coulomb kernel $1/|\mathbf{x} - \mathbf{x}'|$ and \mathcal{I} is the Identity operator. κ_c in this weighted norm definition penalizes the term $\langle \tilde{\rho}_{\text{res}} | \tilde{\rho}_{\text{res}} \rangle$ during the Anderson minimization step at longer wavelength changes of total charge density (i.e. at smaller magnitude of wavevectors, $|\mathbf{q}| \rightarrow 0$ in Fourier representation) in order to suppress charge sloshing in material systems with vanishing bandgaps [56, 74]. Since the objective function (41) in Anderson mixing is non-local in real-space, we now provide a prescription to recast this equation into a local-form using an auxiliary potential corresponding to residual charge density $\tilde{\rho}_{\text{res}}(\mathbf{x})$ -via- the solution of the Poisson problem. To this end, we first note that

$$\begin{aligned} \langle \tilde{\rho}_{\text{res}} | \kappa_c | \tilde{\rho}_{\text{res}} \rangle &= \int \int \frac{\tilde{\rho}_{\text{res}}(\mathbf{x}) \tilde{\rho}_{\text{res}}(\mathbf{x}')}{|\mathbf{x} - \mathbf{x}'|} d\mathbf{x} d\mathbf{x}' \\ &= \int \tilde{\rho}_{\text{res}}(\mathbf{x}) \varphi_{\text{res}}(\mathbf{x}) d\mathbf{x} \end{aligned} \quad (42)$$

where $\varphi_{\text{res}}(\mathbf{x}) = \int \frac{\tilde{\rho}_{\text{res}}(\mathbf{x}')}{|\mathbf{x} - \mathbf{x}'|} d\mathbf{x}'$ denotes the auxiliary potential and is computed by solving the Poisson problem $-\frac{1}{4\pi} \nabla^2 \varphi_{\text{res}}(\mathbf{x}) = \tilde{\rho}_{\text{res}}(\mathbf{x})$. Finally, from this Poisson

equation and Eqn. (42), we have the following

$$\begin{aligned} \langle \tilde{\rho}_{\text{res}} | \kappa_c | \tilde{\rho}_{\text{res}} \rangle &= \int \tilde{\rho}(\mathbf{x}) \varphi_{\text{res}}(\mathbf{x}) d\mathbf{x} = -\frac{1}{4\pi} \int \nabla^2 \varphi_{\text{res}}(\mathbf{x}) \varphi_{\text{res}}(\mathbf{x}) d\mathbf{x}, \\ &= -\frac{1}{4\pi} \int (\nabla \cdot (\varphi_{\text{res}} \nabla \varphi_{\text{res}}) - |\nabla \varphi_{\text{res}}(\mathbf{x})|^2) d\mathbf{x}, \\ &= \frac{1}{4\pi} \int |\nabla \varphi_{\text{res}}(\mathbf{x})|^2 d\mathbf{x}, \end{aligned} \quad (43)$$

where we used the divergence theorem for zeroing out the boundary term to get the last equality in the above equation.

Employing the finite-element discretization for the underlying electronic fields, we solve the following minimization problem in the Anderson mixing scheme.

$$\|\tilde{\rho}_{\text{res}}^h(\mathbf{x})\|_W^2 := \frac{1}{4\pi} \int |\nabla \varphi_{\text{res}}^h(\mathbf{x})|^2 d\mathbf{x} + \int |\tilde{\rho}_{\text{res}}^h(\mathbf{x})|^2 d\mathbf{x} \quad (44)$$

where, $\varphi_{\text{res}}^h(\mathbf{x})$ is the solution of the FE discretized Poisson equation $\mathbf{L} \Phi_{\text{res}} = \mathbf{c}_{\text{res}}$ with \mathbf{L} denoting the discretized Laplacian operator as given in Eqn. (33) and \mathbf{c}_{res} is the forcing vector given by $\int \tilde{\rho}_{\text{res}}^h N_I^{h, \text{pel}} d\mathbf{x}$ while the entries of the solution vector Φ_{res} denotes the linear combination coefficients of the expansion of $\varphi_{\text{res}}^h(\mathbf{x})$ in FE basis. Finally, the Anderson mixing coefficients c_k in Eqn. (40) obtained by minimizing the weighted norm defined in Eq.(44) are employed to determine the input total charge density $\tilde{\rho}_{\text{in}}^{h, (n+1)}$ using Eqn. (39). In other words, the linear combination coefficients c_k are used to determine $\tilde{n}_{\text{in}}^h(\mathbf{x})$ and $\{\mathbf{D}_{\text{in}}^{a, h}\}$ for the subsequent $(n+1)^{\text{th}}$ SCF iteration.

Using $\tilde{\rho}^h(\mathbf{x})$, the Hamiltonian(\mathbf{H}) is computed and subsequently we solve the FE discretized generalized eigenvalue problem $\mathbf{H} \tilde{\mathbf{u}}_i = \varepsilon_i \mathbf{S} \tilde{\mathbf{u}}_i$. The following subsections describes the details of the efficient solution strategies employed in the current work.

B. Subspace iteration procedure for PAW generalised eigenvalue problem

We employ the Chebyshev filtered subspace iteration approach(ChFSI) [23, 60, 75–77] to solve the FE discretized generalized non-linear eigenvalue problem in Eq.(37) for the smallest N eigenvector and eigenvalue pairs. ChFSI belongs to a class of iterative orthogonal projection methods and has been successfully employed in conducting large-scale real space DFT calculations over the past few years [42, 78, 79]. This approach relies on a Chebyshev filtering procedure that constructs a subspace rich in the wanted eigenvectors exploiting the fast growth property of Chebyshev polynomials outside the interval $[-1, 1]$, followed by a Rayleigh-Ritz step. The ChFSI approach can be viewed as a nonlinear subspace iteration procedure in the context of self-consistent field (SCF) iteration employed in solving the DFT nonlinear

eigenvalue problem, allowing the reuse of the filtered subspace V spanned by the eigenvectors of a given SCF iteration to a subsequent iteration progressively improving it. To this end, the eigenspace of interest is refined at every SCF iteration, leading to a close approximation of the desired eigenspace of the non-linear eigenvalue problem as the SCF iterations proceeds towards convergence. Most importantly, the ChFSI method is naturally amenable for efficient use of high-performance computing architectures since the construction of the filtered subspace does not involve any interaction amongst the vectors, allowing for matrix-multivector multiplications to be done block-wise or in parallel over a few blocks, reducing the peak memory requirement [30, 40].

Unlike most of the prior works [23, 76, 78] that employed ChFSI for standard eigenvalue problems, we need to solve here a large sparse generalized Hermitian eigenvalue problem (GHEP) as given in Eqn. (37). In the following, we describe the ChFSI approach adopted in the current work to solve this GHEP arising out of the finite-element (FE) discretization of the PAW method.

a. Construction of Chebyshev filtered subspace: To solve the GHEP in Eqn. (37), we consider the matrix $\mathbf{S}^{-1}\mathbf{H}$ that has the same eigenpairs as $\mathbf{H}\tilde{\mathbf{u}} = \epsilon\mathbf{S}\tilde{\mathbf{u}}$. To amplify the eigenspace of the interest corresponding to the N smallest eigenvectors (wanted spectrum) and dampen the unwanted spectrum, we seek to construct a Chebyshev polynomial filter involving $\mathbf{S}^{-1}\mathbf{H}$. This requires us to efficiently evaluate the inverse of \mathbf{S} , a large FE discretized sparse matrix. We now recall from Eq. (36) that \mathbf{S} is of the form $\mathbf{S} = \mathbf{M} + \mathbf{P}\Delta_{\mathbf{s}}\mathbf{P}^\dagger$, a rank- n_{proj} perturbation of \mathbf{M} . We now use the Woodbury formula [80] to compute the inverse of \mathbf{S} , that can be expressed as

$$\mathbf{S}^{-1} = \mathbf{M}^{-1} - \mathbf{M}^{-1}\mathbf{P}\Delta_{\mathbf{s}_{\text{inv}}}\mathbf{P}^\dagger\mathbf{M}^{-1} \quad (45)$$

where $\Delta_{\mathbf{s}_{\text{inv}}} = \left(\Delta_{\mathbf{s}}^{-1} + \mathbf{P}^\dagger\mathbf{M}^{-1}\mathbf{P}\right)^{-1}$

We note that the above Equation (45) requires the computation of inverse of the large $M \times M$ sparse FE basis overlap-matrix (\mathbf{M}), and the inverse of a smaller matrix $\left(\Delta_{\mathbf{s}}^{-1} + \mathbf{P}^\dagger\mathbf{M}^{-1}\mathbf{P}\right)$ of size $n_{\text{proj}} \times n_{\text{proj}}$ that scales with number of atoms. To evaluate \mathbf{M}^{-1} , Gauss-Lobatto-Legendre (GLL) quadrature rules coincident with the finite-element nodes of spectral finite-elements are employed in this work. These GLL points are reduced-order quadrature rules and are used only to construct \mathbf{M} in Eqn. (32), rendering the matrix \mathbf{M} diagonal denoted by \mathbf{M}_D . This leads to a trivial evaluation [23, 42] of \mathbf{M}^{-1} by inverting the diagonal entries of \mathbf{M}_D to be denoted as \mathbf{M}_D^{-1} in the subsequent text. The other term in \mathbf{S}^{-1} which needs careful treatment, is the inverse of $\left(\Delta_{\mathbf{s}}^{-1} + \mathbf{P}^\dagger\mathbf{M}^{-1}\mathbf{P}\right)$. Recall from Eqns. (35) and (36), $\Delta_{\mathbf{s}}$ is block diagonal with each block corresponding to each atom 'a' and hence $\Delta_{\mathbf{s}}^{-1}$ can be evaluated as the inverse of individual blocks $\Delta_{\mathbf{s}}^a$. Furthermore, using the fact that the PAW augmentation spheres are localized in

real-space and seldom overlap, the matrix $\mathbf{P}^\dagger\mathbf{M}_D^{-1}\mathbf{P}$ can be approximated as a block diagonal matrix with each block corresponding to an atom in the given material system. Hence, the block diagonal form of the $\Delta_{\mathbf{s}_{\text{inv}}}^a$ matrix in real-space allows us to compute its inverse atom-by-atom. To this end, the approximate \mathbf{S}^{-1} can be recast as follows:

$$\hat{\mathbf{S}}^{-1} = \mathbf{M}_D^{-1} - \sum_a \mathbf{M}_D^{-1}\mathbf{C}^a\Delta_{\mathbf{s}_{\text{inv}}}^a\mathbf{C}^{a\dagger}\mathbf{M}_D^{-1} \quad (46)$$

$$\text{where } \Delta_{\mathbf{s}_{\text{inv}}}^a = \left(\Delta_{\mathbf{s}}^{a^{-1}} + \mathbf{C}^{a\dagger}\mathbf{M}_D^{-1}\mathbf{C}^a\right)^{-1}$$

In this work, we seek to construct a subspace rich in the desired eigenvectors of the PAW generalized eigenvalue problem $\mathbf{H}\tilde{\mathbf{u}} = \epsilon\mathbf{S}\tilde{\mathbf{u}}$ in Eqn. (37) by building a Chebyshev polynomial filter of $\hat{\mathbf{H}} = \hat{\mathbf{S}}^{-1}\mathbf{H}$ a close approximation to $\mathbf{S}^{-1}\mathbf{H}$. To this end, the filtering procedure first relies on mapping the unwanted spectrum of $\hat{\mathbf{H}}$ to $[-1, 1]$ and the desired spectrum to $(-\infty, -1)$. This is accomplished by computing a shifted and scaled matrix $\tilde{\mathbf{H}}$ through the affine transformation given by $\tilde{\mathbf{H}} = \frac{2}{b-a}\hat{\mathbf{H}} - \frac{b+a}{b-a}\mathbf{I}$ where a and b denote the upper bounds of occupied and unoccupied spectrum respectively. The upper bound b of the unwanted spectrum is obtained inexpensively by using a few steps of generalized Lanczos iteration [81] as discussed in the Algorithm (2) which employs $\hat{\mathbf{S}} = \mathbf{M}_D + \sum_a \mathbf{C}^a\Delta_{\mathbf{s}}^a\mathbf{C}^{a\dagger}$ and its inverse $\hat{\mathbf{S}}^{-1}$ as discussed in Eqn. (46). A good approximation to the upper bound a of the wanted spectrum is obtained as the highest generalized Rayleigh quotient of $\tilde{\mathbf{H}}$ in the Chebyshev filtered subspace of the previous SCF iteration. We now construct the filtered subspace by computing the action of a degree- m Chebyshev polynomial filter $T_m(\tilde{\mathbf{H}})$ on an input subspace $\tilde{\Psi}_{\text{in}}$ where the subspace $\tilde{\Psi}_{\text{in}}$ is usually the eigenspace from the previous SCF iteration and is a matrix of size $M \times N$. This action is accomplished -via- the three-term recurrence relation of Chebyshev polynomials as given below:

$$\tilde{\Psi}_{\text{f}} = T_m(\tilde{\mathbf{H}})\tilde{\Psi}_{\text{in}} \text{ where } T_{m+1}(\mathbf{X}) = 2\mathbf{X}T_m(\mathbf{X}) - T_{m-1}(\mathbf{X})$$

The rapid growth property of Chebyshev polynomials outside $[-1, 1]$ amplifies the components in $\tilde{\Psi}_{\text{in}}$ along the direction of the desired eigenvectors (occupied states) while dampening the components along the unwanted eigenvectors (unoccupied states), leading to the filtered subspace $\tilde{\Psi}_{\text{f}}$ to be a close approximation of the eigenspace of interest of the PAW eigenproblem $\mathbf{H}\tilde{\mathbf{u}} = \epsilon\mathbf{S}\tilde{\mathbf{u}}$ in a given SCF iteration.

b. Rayleigh-Ritz step: Upon computing the filtered subspace $\tilde{\Psi}_{\text{f}}$ in a given SCF iteration, we project the Hamiltonian (\mathbf{H}) and PAW-overlap (\mathbf{S}) onto the filtered subspace $\tilde{\Psi}_{\text{f}}$ to construct projected matrices \mathbf{H}^p and \mathbf{S}^p of size $N \times N$ as shown in step 5 of algo.(3). The Rayleigh-Ritz step now involves solving a subspace eigen-

Algorithm 2: k -step generalized Lanczos iteration

- Output:** Estimate of b the upper bound of unoccupied spectrum of $\mathbf{H}\tilde{\mathbf{u}} = \epsilon\hat{\mathbf{S}}\tilde{\mathbf{u}}$
1. Choose random vector \mathbf{v}_0 , such that $\|\mathbf{v}_0\|_{\hat{\mathbf{S}}} = 1$, where $\|\mathbf{v}\|_{\hat{\mathbf{S}}} = (\mathbf{v}^*\hat{\mathbf{S}}\mathbf{v})^{\frac{1}{2}}$
 2. Compute entries of $k \times k$ tridiagonal Hessenberg matrix \mathbf{T} whose entries are $T_{i,i} = \alpha_i$ and $T_{i+1,i} = T_{i,i+1} = \beta_i$ as follows:
 3. $\alpha_1 = (\mathbf{v}_0^*\mathbf{H}\mathbf{v}_0)$
 4. $\mathbf{u}_0 = \hat{\mathbf{S}}^{-1}\mathbf{H}\mathbf{v}_0 - \alpha_1\mathbf{v}_0$
 5. for $i = 1$ to k do
 - $\beta_i = \|\mathbf{u}_{i-1}\|_{\hat{\mathbf{S}}}$
 - $\mathbf{v}_i = \frac{1}{\beta_i}\mathbf{u}_{i-1}$
 - $\mathbf{u}_i = \hat{\mathbf{H}}\mathbf{v}_i - \beta_i\mathbf{v}_{i-1}$
 - $\alpha_i = (\mathbf{v}_i^*\mathbf{H}\mathbf{v}_i)$
 - $\mathbf{u}_i = \mathbf{u}_i - \alpha_i\mathbf{v}_i$
 6. compute λ_T^{\max} the max eigenvalue of \mathbf{T}
 7. $\beta_{k+1} = \|\mathbf{u}_i\|_{\hat{\mathbf{S}}}$
 8. $b = \lambda_T^{\max} + \beta_{k+1}$
-

value problem for N eigenpairs and is of the form

$$\mathbf{H}^p\mathbf{X} = \mathbf{S}^p\mathbf{X}\mathbf{\Lambda} \quad (47)$$

where \mathbf{X} and $\mathbf{\Lambda}$ denote the eigenvector matrix and the diagonal eigenvalue matrix of the smaller subspace eigenvalue problem Eqn.(47) respectively. Finally, a subspace rotation step (see step 7 of Algo.(3)) is carried out to obtain the \mathbf{S} -orthonormal eigenvectors $\tilde{\Psi}$ in the finite-element subspace which is in turn used to compute the output total charge density $\tilde{\rho}^h(\mathbf{x}) = \tilde{n}^h + \tilde{b}(\mathbf{x})$.

A good approximation to the eigenspace of interest in the ChFSI approach employed in this work relies on the choice of the degree m of the Chebyshev polynomial filter. This choice depends on the separation of eigenvalues within the desired region of eigenspectrum and also, the magnitude of the largest eigenvalue (λ_{\max}) of the matrix $\mathbf{S}^{-1}\mathbf{H}$ that determines the ratio of spectral widths of the wanted to the unwanted regions of the eigenspectrum. We note that this λ_{\max} is dictated by the fineness of the mesh size of the underlying finite-element discretization, i.e., it increases with decreasing mesh size. In the PAW method within the frozen core approximation, the electronic fields $\{\tilde{\psi}_i\}$ (or equivalently $\{\tilde{u}_i^{\mathbf{k}}\}$ in the periodic case) and φ vary smoothly compared to the electronic fields in the case of ONCV pseudopotentials for most atomic species. This allows for the use of coarser finite-element meshes in the case of PAW formalism, leading to the choice of Chebyshev polynomial degree between 10 and 30 for accurately approximating the desired eigenspace. The reduced degrees of freedom and the lower Chebyshev polynomial degree required to reach

the desired chemical accuracies in the proposed finite-element framework for the PAW approach gives four to five fold computational advantage compared to current state-of-the-art finite-element code for DFT using ONCV pseudopotentials (DFT-FE) as will be demonstrated in the subsequent sections.

The ChFSI approach described here involves computational intensive operations notably in two key steps: first, constructing a subspace by computing $\mathbf{A}\mathbf{X}$, where \mathbf{A} represents any one of the matrices \mathbf{S} , \mathbf{H} , $\hat{\mathbf{S}}^{-1}$, and second, performing a Rayleigh-Ritz step by computing matrix-matrix products of the form $\mathbf{X}^\dagger\mathbf{Y}$. We will now elucidate efficient strategies that exploit the compact support nature of the finite-element basis to evaluate these operations in a computationally efficient manner.

Algorithm 3: ChFSI algorithm in PAW-FE

- Input:** Initial subspace $\tilde{\Psi}_{\text{in}}$
- Output:** \mathbf{S} -orthonormalised filtered subspace $\tilde{\Psi}$
1. Compute b from k -step Generalized Lanczos as per Algorithm (2)
 2. Determine the upper bound of wanted and unwanted spectrum
 3. Scale and shift the Hamiltonian:
 $\hat{\mathbf{H}} = \frac{2}{b-a}\hat{\mathbf{H}} - \frac{b+a}{b-a}\mathbf{I}$, where $\hat{\mathbf{H}} = \hat{\mathbf{S}}^{-1}\mathbf{H}$
 4. Compute Chebyshev filtered subspace:
 $\tilde{\Psi}_f = T_m(\hat{\mathbf{H}})\tilde{\Psi}_{\text{in}}$
 5. **RR-Projection** Compute the projected Hamiltonian (\mathbf{H}^p) and projected PAW overlap matrices (\mathbf{S}^p) as:
 $\mathbf{H}^p = \tilde{\Psi}_f^\dagger\mathbf{H}\tilde{\Psi}_f$, $\mathbf{S}^p = \tilde{\Psi}_f^\dagger\mathbf{S}\tilde{\Psi}_f$
 6. **RR-GHEP** Solve the GHEP: $\mathbf{H}^p\mathbf{X} = \mathbf{S}^p\mathbf{X}\mathbf{\Lambda}$
 7. **RR-SR** Perform subspace rotation: $\tilde{\Psi} = \tilde{\Psi}_f\mathbf{X}$.
-

C. Efficient computational methodologies

In the proposed ChFSI approach in Algorithm (3), the efficient computation of matrix-matrix products of the form $\mathbf{A}\mathbf{X}$ and $\mathbf{X}^\dagger\mathbf{Y}$ is critical for enabling fast, accurate and scalable PAW-FE calculations on parallel computing architectures. We first consider the case of evaluating the matrix multivector products of the form $\mathbf{A}\mathbf{X}$ arising in the construction of Chebyshev filtered subspace, where the matrix \mathbf{A} can be one of discretized Hamiltonian matrix(\mathbf{H}), PAW overlap(\mathbf{S}) matrix or its inverse. We note here that the matrix \mathbf{A} is a large sparse matrix of dimension $M \times M$ with $M \approx \mathcal{O}(10^3) - \mathcal{O}(10^8)$ while \mathbf{X} is a large dense matrix of dimension $M \times N$ with $N \approx \mathcal{O}(10) - \mathcal{O}(10^4)$. A naive strategy often adopted in the finite-element literature to compute $\mathbf{A}\mathbf{X}$ would be to construct the FE discretized global sparse matrix \mathbf{A} using sparse-matrix storage data-structures and then compute the sparse matrix-dense matrix product $\mathbf{A}\mathbf{X}$ []. This strategy would be highly inefficient on mod-

ern parallel computing systems involving multi-threaded and multi-node architectures owing to the expensive data movement costs involved in the underlying sparse-matrix algorithms. To this end, we employ a cell-matrix approach [29, 39, 42, 82] that avoids the construction of global sparse-dense matrix-products and instead employs dense-dense matrix-products at FE cell level to reduce memory requirements, enhance cache locality, and improve arithmetic intensity of computation. We describe below the key mathematical aspects used in this implementation strategy to efficiently evaluate \mathbf{AX} during the ChFSI procedure in solving the PAW generalized eigenvalue problem.

Denoting the simulation domain by Ω_p , we begin by partitioning Ω_p into subdomains $\Omega^{(t)} \forall t = 1, 2, \dots, n_t$, where n_t is the number of subdomains with each subdomain $\Omega^{(t)}$ assigned to an MPI task t . Further, let E_t be the number of finite-element (FE) cells and m_t be the number of basis functions (number of finite-element nodes) in each subdomain $\Omega^{(t)}$ such that $\Omega^{(t)} = \cup_{e=1}^{E_t} \Omega^{(e,t)}$, where the notation (e, t) refers to the index of the FE cell 'e' in an MPI task 't'. This allows us to decompose the integrals over the domain Ω_p in Eqs (31), (32) to a series of integrals over smaller domains $\Omega^{(e,t)}$ as

$$\int_{\Omega_p} d\mathbf{x} = \sum_t \sum_e \int_{\Omega^{(e,t)}} d\mathbf{x} \quad (48)$$

Finally, the integrals over each domain $\Omega^{(e,t)}$ are computed using a suitable quadrature rule as:

$$\int_{\Omega^{(e,t)}} f(\mathbf{x}) d\mathbf{x} = \sum_q^{N_q} f(\mathbf{x}_q) w_q \quad (49)$$

where N_q is the total number of quadrature points in the domain $\Omega^{(e,t)}$ while w_q, \mathbf{x}_q are the quadrature weights and sampling points respectively. 3D Gauss Legendre quadrature rules that are tensor products of 1D quadrature rules [83] are employed in this work, and the order of these rules employed are determined such that errors due to the quadrature rule are of higher order than the discretization error (details of the selection procedure are discussed in supplementary information). The flexibility in the choice of quadrature rules for evaluating various integrals involving PAW atomic data in Eqns 17 allows the use of coarser finite-element grids to represent electronic fields and yet capture the relevant atom-centered data, a notable advantage compared to finite-difference approach, a popular real-space discretization DFT method, where special schemes need to be devised to retain the use of coarser grid resolution for smoother electronic fields without egg-box effects [84].

We note that the operation \mathbf{AX} can be decomposed as $\mathbf{AX} = \mathbf{A}_{\text{loc}}\mathbf{X} + \mathbf{A}_{\text{nlloc}}\mathbf{X}$ (where $\mathbf{A} := \mathbf{H}, \mathbf{S}, \hat{\mathbf{S}}^{-1}$ and $\mathbf{A}_{\text{loc}} := \mathbf{H}_{\text{loc}}, \mathbf{M}, \mathbf{M}_{\text{D}}^{-1}$ respectively). To this end, the mathematical expressions for \mathbf{AX} relevant to our implementation strategy within the finite-element framework can be written as

$$\mathbf{HX} = \left[\sum_t^{n_t} \mathbf{B}^{(t)T} \mathbf{Q}^{(t)T} \sum_e^{E_t} \mathbf{Z}^{(e,t)T} \left(\mathbf{H}_{\text{loc}}^{(e,t)} + \sum_a \mathbf{C}^{(a,e,t)} \Delta_{\mathbf{H}}^a \left(\sum_{t^a} \sum_{e^a} \mathbf{C}^{(a,e^a,t^a)\dagger} \delta_{e^a e} \delta_{t^a t} \right) \right) \mathbf{Z}^{(e,t)} \mathbf{Q}^{(t)} \mathbf{B}^{(t)} \right] \mathbf{X} \quad (50)$$

$$\mathbf{SX} = \left[\sum_t^{n_t} \mathbf{B}^{(t)T} \mathbf{Q}^{(t)T} \sum_e^{E_t} \mathbf{Z}^{(e,t)T} \left(\mathbf{M}^{(e,t)} + \sum_a \mathbf{C}^{(a,e,t)} \Delta_{\mathbf{S}}^a \left(\sum_{t^a} \sum_{e^a} \mathbf{C}^{(a,e^a,t^a)\dagger} \delta_{e^a e} \delta_{t^a t} \right) \right) \mathbf{Z}^{(e,t)} \mathbf{Q}^{(t)} \mathbf{B}^{(t)} \right] \mathbf{X} \quad (51)$$

$$\hat{\mathbf{S}}^{-1} \mathbf{X} = \mathbf{M}_{\text{D}}^{-1} \mathbf{X} - \left[\sum_t^{n_t} \mathbf{B}^{(t)T} \mathbf{Q}^{(t)T} \sum_e^{E_t} \mathbf{Z}^{(e,t)T} \mathbf{M}_{\text{D}}^{-1(e,t)} \sum_a \mathbf{C}^{(a,e,t)} \Delta_{\mathbf{S}_{\text{inv}}}^a \left(\sum_{t^a} \sum_{e^a} \mathbf{C}^{(a,e^a,t^a)\dagger} \delta_{e^a e} \delta_{t^a t} \right) \mathbf{Z}^{(e,t)} \mathbf{Q}^{(t)} \mathbf{B}^{(t)} \right] \mathbf{M}_{\text{D}}^{-1} \mathbf{X} \quad (52)$$

In the Eqns.(50)-(52), the Boolean sparse matrix $\mathbf{B}^{(t)}$ represents the **partitioner matrix** that acts on \mathbf{X} (or $\mathbf{M}_{\text{D}}^{-1} \mathbf{X}$) to provide the subdomain level matrix $\mathbf{X}^{(t)}$ while preserving the continuity of the nodal field across the subdomain boundaries. The $m_t \times m_t$ sparse matrix $\mathbf{Q}^{(t)}$ represents the **constraint matrix** that constrains the values of the $m_t \times N$ matrix $\mathbf{X}^{(t)}$ at the specific FE nodes.

These constraints either satisfy the necessary boundary conditions (periodic, non-periodic, or semi-periodic) imposed on the discretized electronic wavefunctions or address constraints from non-conforming meshes [85]. Furthermore, the $n_p^3 \times m_t$ Boolean matrix $\mathbf{Z}^{(e,t)}$ denotes the **sub-domain to FE cell map** associated with the subdomain Ω^t whose action on $\mathbf{Q}^{(t)} \mathbf{X}^{(t)}$ results in the extrac-

tion of the finite-element cell-level entries from $\mathbf{Q}^{(t)}\mathbf{X}^{(t)}$ while ensuring the continuity condition of the discretized electronic wavefunction across the finite-element cells within the partitioned sub-domain $\Omega^{(e,t)}$. Efficient computation of $\mathbf{A}\mathbf{X}$ illustrated in Eqns.(50)-(52) can be summarized as a sequence of the following steps:

- (i) Precompute the entries of the cell-level matrices $\mathbf{H}_{\text{loc}}^{(e,t)}$, $\mathbf{S}_{\text{loc}}^{(e,t)}$, $\mathbf{C}^{(a,e)}$ and $\Delta_{\mathbf{A}}^a$, the atom dependent coupling matrices ($\Delta_{\mathbf{A}}^a := \Delta_{\mathbf{H}}^a, \Delta_{\mathbf{S}}^a, \Delta_{\mathbf{S}_{\text{inv}}}^a$) using the quadrature rules as discussed in Eqns.(48) and (49))
- (ii) Extract the finite-element cell-level matrix:
 $\mathbf{X}^{(e,t)} = \mathbf{Z}^{(e,t)}\mathbf{Q}^{(t)}\mathbf{B}^{(t)}\mathbf{X}, \forall (e, t)$
- (iii) Evaluate the partial non-local operator action at the FE cell level:
 $\Delta_{\mathbf{Y}}^a = \sum_{t^a} \sum_{e^a} \mathbf{C}^{(a,e^a,t^a)\dagger} \delta_{e^a e} \delta_{t^a t} \mathbf{X}^{(e,t)}$ where $\delta_{e^a e}$ indicates that this computation is done in only those FE cells e^a lying in the augmentation sphere (Ω_a) centered around an atom ' a '. Furthermore, $\delta_{t^a t}$ indicates that this computation is done only on those MPI tasks t^a which are associated with Ω_a .
- (iv) Evaluate the local operator action along with the impending non-local operator action:
 $\mathbf{Y}^{(e,t)} = \mathbf{A}_{\text{loc}}^{(e)}\mathbf{X}^{(e,t)} + \sum_a \mathbf{C}^{(a,e,t)}\Delta_{\mathbf{A}}^a\Delta_{\mathbf{Y}}^a$
- (v) Assembly of the global vector $\mathbf{Y} = \mathbf{A}\mathbf{X}$:
 $\mathbf{Y} = \sum_t^{n_t} \mathbf{B}^{(t)T} \mathbf{Q}^{tT} \sum_e^{E_t} \mathbf{Z}^{(e,t)T} \mathbf{Y}^{(e,t)}$

We remark that the finite-element cell-level matrices $\mathbf{H}_{\text{loc}}^{e,t}$ and the coupling matrix $\Delta_{\mathbf{H}}^a$ are computed at every SCF iteration while $\mathbf{S}_{\text{loc}}^{e,t}$ is computed for a given finite-element mesh. Further $\Delta_{\mathbf{S}}^a$ is computed only once while $\Delta_{\mathbf{S}_{-1}}^a$ is evaluated only once per ground-state calculation.

Following the evaluation of $\mathbf{Y} = \mathbf{A}\mathbf{X}$, the key computationally intensive operation in the construction of Chebyshev filtered subspace, the subsequent step is the Rayleigh-Ritz step that requires the evaluation of matrix-matrix products of the form $\mathbf{X}^\dagger\mathbf{Y}$ (see Algorithm 3). To this end, the matrices \mathbf{X}, \mathbf{Y} are partitioned row wise into $\mathbf{X}_p, \mathbf{Y}_p$ across various MPI tasks without ensuring continuity of the nodal field. To this, the local $\mathbf{X}_p^\dagger\mathbf{Y}_p$ is evaluated to obtain the smaller matrix $N \times N$ in each MPI tasks and finally, the local contribution is summed up across all MPI tasks to obtain $\mathbf{X}^\dagger\mathbf{Y} = \sum_p \mathbf{X}_p^\dagger\mathbf{Y}_p$.

So far, in this section we discussed the various computational methodologies employed in the proposed PAW-FE approach that can enable accurate large-scale DFT calculations on material systems up to tens of thousands of electrons in a computationally efficient manner. The following section discusses the accuracy and performance results of the proposed computational approach while benchmarking with state-of-the-art plane Wave(PW) codes Abinit[86] and Quantum Espresso[53].

V. RESULTS AND DISCUSSION

In this section, we demonstrate the accuracy, performance and parallel scalability of the proposed method PAW-FE on representative benchmark problems involving periodic, semi-periodic and non-periodic boundary conditions. We first discuss the accuracy of our implementation on non-periodic systems involving molecular systems and small metallic nano-clusters by comparing energetics with plane-wave-based PAW implementations. We then demonstrate the performance of PAW-FE in terms of both computational node hours and minimum wall time with respect to plane-wave calculations for increasingly large sizes of metallic Cu nanoclusters containing up to 17537 electrons (923 atoms). Subsequently, we demonstrate the accuracy of our method compared to plane-wave calculations on semi-periodic and fully periodic systems involving unit-cells, large super-cells, surfaces. We further discuss the performance of our method in terms of computational node-hrs and minimum wall time for increasingly large sizes of Cu₃Pt periodic supercells containing up to 34,304 electrons (2048 atoms) compared to plane-wave DFT calculations using PAW. Finally, we showcase the computational efficiency and parallel scalability of PAW-FE compared to norm-conserving ONCV pseudopotential DFT calculations using DFT-FE on large-scale material systems involving $\sim 50,000$ electrons.

All the DFT calculations reported in this work employ GGA [65] exchange-correlation functional of the PBE [87] form. Further, we employ the PAW data-sets from the pseudo-dojo database [88, 89]. In all our simulations, we use Fermi-Dirac smearing with $T = 500K$. Additionally, for the mixing of the total charge density involving $(\tilde{n}(\mathbf{x}))$ and $\{\mathbf{D}^a\}$, we employ the n-stage Anderson mixing [73] as discussed in the Section IV.

For all accuracy validation studies in this work, we employ refined finite element (FE) meshes with FE interpolating polynomial (p) of degree 7. These meshes are constructed such that the differences in the all-electron ground-state energies (Eqn. (18)) between successively sub-divided meshes reach $\mathcal{O}(10^{-6})$ Ha/atom. In addition, the choice of quadrature integration rules and FE interpolating polynomial for electrostatics p_{el} is chosen such that the energy variation with respect to these parameters is an order of magnitude lower than this discretization error. In the case of plane-wave calculations we use ABINITcode and the cut-off energy for wavefunctions $E_{\text{cut}}^{\text{wfc}}$ is chosen so that the ground-state energy is converged up to $\mathcal{O}(10^{-6})$ Ha/atom while simultaneously ensuring that energy change with respect to the cut-off energy for total charge density $E_{\text{cut}}^{\text{rho}}$ is an order of magnitude lower.

The comparative study involving the performance of our PAW-FE implementation with that of plane-wave calculations has been conducted by solving a given DFT problem to the same level of accuracy. To this end, we choose the discretization parameters such that the discretization error with respect to a very refined calcu-

lation in each case to be around $\sim 2 \times 10^{-4}$ Ha/atom for our comparisons. We employ **Quantum espresso(QE)** code for conducting our performance studies using plane-wave DFT calculations. Furthermore, we use two metrics to compare the performance of PAW-FE and the plane-wave calculations: (i) computational cost (η_c) in node-hrs, and (ii) minimum wall time (τ_c^{\min}) in secs. The computational cost η_c is obtained by multiplying the minimum number of compute nodes required to fit a given problem with the average wall-time per SCF iteration¹. Further, the minimum wall time (τ_c^{\min}) is obtained by computing average wall time per SCF by increasing the number of compute nodes till a parallel scaling efficiency of around 35% is reached. All the simulations involved in the accuracy and performance benchmarking studies were performed on high-memory CPU nodes of PARAM Pravega².

A. Non-periodic systems

In this subsection, we consider the case of non-periodic systems for our accuracy and performance benchmarking. In particular, for accuracy validation studies, we consider isolated molecules such as CO, CH₄, H₂O and also metallic nano-clusters such as Cu₁₃, Al₁₃. We benchmark the accuracy of PAW-FE with ABINIT by comparing the energy vs bond length curves and the ground state energies computed at the minimum energy configuration. Following the accuracy validation study, we assess the performance of our implementation by comparing the computational cost (η_c) and minimum wall time (τ_c^{\min}) of PAW-FE with Quantum Espresso(QE), a widely used code employing plane-wave basis. In this performance benchmarking study, we consider three-dimensional icosahedron[90] shaped Cu nanoparticles of various sizes ranging from 55 atoms (1045 electrons) to 923 atoms (17537 electrons). Homogeneous boundary conditions have been imposed on the electrostatic potential ($\phi^h(\mathbf{x})$) for these calculations using PAW-FE while in plane-wave codes, periodic boundary conditions (PBCs) are only admissible and hence PBCs are employed using a suitable vacuum to minimise image-image interactions.

1. Accuracy benchmarking

In all the accuracy benchmarking studies reported in this subsection, we choose refined finite-element (FE) meshes with FE interpolating polynomial degree p to be 7 and the mesh size h to be around 1.0 Bohr while in the case of ABINIT³, we use a plane-wave cut-off energy $E_{\text{cut}}^{\text{wfc}} = 60$ Ha. Figure (1) reports the energy as a function of inter-atomic distance obtained from ABINIT and PAW-FE for the molecular systems O₂, H₂O, NH₃ and CH₄. Since the scale of ground-state energies is different in the two implementations compared here, the energies in the plots of Fig. (1) are measured relative to the minimum ground-state energy obtained in this study using ABINIT and PAW-FE for each of the above molecular systems. We now describe the details of the simulations conducted for our comparative study: (i) *Oxygen*: The energy as a function of O-O bond length is plotted in Fig. (1)(a) and the bond length for the minimum energy configuration is found to be 2.30 Bohr in PAW-FE which is in excellent agreement with ABINIT, (ii) *Ammonia*: The trigonal pyramidal geometry of ammonia is considered where the N-H bond lengths are varied such that the H-N-H bond angle is maintained to be 106.2°. In the Fig. (1)(b), we plot the energy variation as a function of this N-H bond length and we observe the N-H bond length at the minimum energy configuration to be around 1.93 Bohr using PAW-FE which matches very closely to the value obtained with ABINIT, (iii) *Water*: The O-H bond lengths in the water molecule are varied while ensuring that the planar H-O-H bond angle of 104.46° is maintained. Energy of the molecule is plotted as a function of this O-H bond length in Fig. (1)(c) and we observe from our PAW-FE calculations that the O-H bond length at the minimum energy configuration is 1.83 Bohr which is in close agreement with ABINIT, (iv) *Methane*: The tetrahedral geometry of methane is considered where the C-H bond lengths are varied such that H-C-H angle is maintained at 109.5°. Fig. (1) (d) shows the comparison between PAW-FE and ABINIT calculations. These results indicate that the C-H bond length at the minimum energy configuration is 2.07 Bohr in both cases.

To summarize the observations from Fig. (1), we find an excellent agreement in all the energy vs bond-length curves between PAW-FE and ABINIT for the representative molecules considered in this work. Furthermore, the bond length at the minimum energy configuration obtained from our implementation shows a very close match with that of plane-wave calculations as summarized in Table I. We now compare the ground-state energies of a few representative systems obtained using PAW-FE with that of ABINIT in TableII. To this end, we consider the

¹ Average wall-time per SCF is obtained by dividing the wall time taken for the self-consistent field iteration procedure with the number of SCF iterations taken to reach a default convergence threshold for self-consistency

² PARAM Pravega is one of India's fastest supercomputers stationed at Indian Institute of Science comprising of 156 High Memory Intel Xeon Cascade-Lake based CPU nodes (7,488 Cores) where each node consists of 48 Intel Xeon 6248 processor, 768 GB memory and Mellanox HDR Infiniband interconnect between all the nodes for fast MPI communication.

³ . We use the `usxcnhat=0` in ABINIT to enforce Blöchl formulation of exchange-correlation(XC) contribution with `pawxcdev=0` to avoid any approximation in the XC correction term computation.

Molecule	Bond Type	Bond length (Bohr)PAW-FE	Bond length (Bohr)ABINIT
O ₂	O-O	2.30	2.30
H ₂ O	O-H	1.83	1.83
NH ₃	N-H	1.93	1.93
CH ₄	C-H	2.07	2.07

TABLE I: Comparison of bond length at the minimum energy configuration between ABINIT and PAW-FE for O₂, H₂O, NH₃ and CH₄ obtained from Fig.(1).

above four molecular systems at the minimum energy configuration obtained from Fig. 1. Additionally, we consider the 13-atom icosahedron nanoclusters Cu₁₃ and Al₁₃ with 4.8 Bohr and 5.3 Bohr as the nearest neighbour distance, respectively [91]. To have a one-on-one comparison of ground-state energies with ABINIT for these non-periodic systems considered in this work, we compute pseudo valence energy. We note that Table(II) shows an excellent match between the ground-state energies obtained from PAW-FE and ABINIT, and the differences in the energies are $O(10^{-5}) \frac{\text{Ha}}{\text{atom}}$. Having established the agreement of PAW-FE with a plane-wave code in terms of energetics, we now focus on performance benchmarking of PAW-FE against the plane-wave implementations.

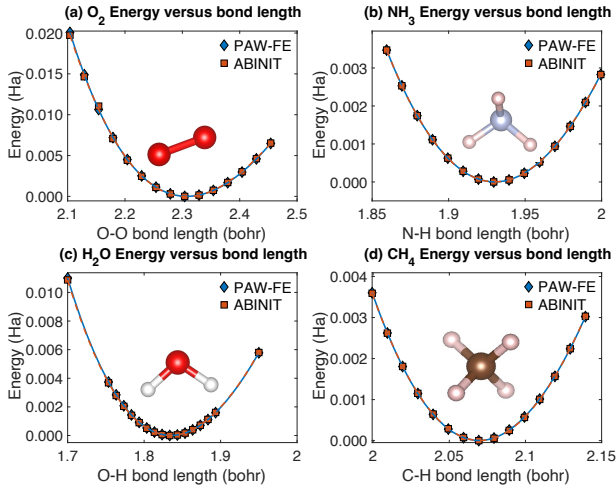


FIG. 1: Comparison between ABINIT and PAW-FE: Energy vs bond length for (a) Oxygen (b) Ammonia (c) Water (d) Methane. The energy shown is relative to the minimum ground-state energy obtained in each code.

System	Abinit Energy (Ha/atom)	PAW-FE Energy (Ha/atom)	Error in Energy (Ha/atom)
H ₂ O	-5.7771402	-5.7771352	4.96×10^{-6}
NH ₃	-2.9544162	-2.9544196	3.39×10^{-6}
O ₂	-16.0550787	-16.0550659	1.28×10^{-5}
CH ₄	-1.6254853	-1.6254649	2.04×10^{-5}
Cu ₁₃	-197.9146105	-197.9146504	4.0×10^{-5}
Al ₁₃	-2.0699280	-2.0699363	8.37×10^{-6}

TABLE II: Ground state energy comparison between ABINIT and PAW-FE for the molecular systems (H₂O, NH₃, O₂, CH₂) and nanoclusters (Cu₁₃, Al₁₃).

2. Performance benchmarking

We benchmark the performance of PAW-FE with Quantum espresso QE[53], a widely used open-source plane-wave (PW) code, by comparing the average CPU time per SCF in terms of computational node-hrs(η_c) and minimum wall time(τ_c^{\min}) with increasing sizes of Cu nanoclusters[90] solved to similar level of accuracy between the two approaches. These icosahedron-shaped nanoclusters considered in this study are constructed with 4.8 Bohr nearest neighbour distance[91], and the nanocluster size is increased by varying the number of shells. To this end, non-periodic DFT calculations using the PAW method are conducted on Cu_{3-shell} (2793 electrons), Cu_{4-shell} (5871 electrons), Cu_{5-shell} (10,659 electrons), Cu_{6-shell} (17,537 electrons). The two metrics (η_c, τ_c^{\min}) used to benchmark the performance results are discussed at the beginning of this section. In PAW-FE, the degree of the FE interpolating polynomial p is chosen to be 5, and a mesh size $h = 1.2$ Bohr is employed, while in the case of QE, the plane-wave cut-off energy $E_{\text{cut}}^{\text{wfc}} = 25\text{Ha}$ is used with Γ -point for k -point sampling. These discretization parameters are chosen such that the discretization error in ground-state energies obtained in both PAW-FE and QE is $\sim 2 \times 10^{-4} \frac{\text{Ha}}{\text{atom}}$. Additionally, we use a vacuum of around 20 Bohr and 15 Bohr from the farthest atom of the nanocluster in PAW-FE and QE respectively, ensuring that ground-state energies are converged up to $O(10^{-5}) \frac{\text{Ha}}{\text{atom}}$ with vacuum size.

Table (III) reports the average CPU time per SCF iteration in terms of computational node-hrs (η_c) and the number of basis functions in PAW-FE and QE for various sizes of Cu nanoclusters studied here. From this table, we find that for system sizes greater than ~ 1000 electrons, PAW-FE becomes more efficient than QE. We observe the efficiency gains for PAW-FE increases with system size over QE, achieving gains of around $3.1\times$, $4.3\times$ and $5.1\times$ for Cu_{4-shell}, Cu_{5-shell} and Cu_{6-shell} respectively, the benchmark systems considered for CPU-time comparison. This increase in computational gains is attributed to the need for using more processors to satisfy the peak memory requirement, where the efficient parallel scalability of PAW-FE provides the necessary advantage. Further, in this case of non-periodic systems, the spatial adaptivity

System	atoms	electrons	QE #basis fns.	QE(η_c) Node-hrs	PAW-FE #basis fns.	PAW-FE(η_c) Node-hrs	Speed-up
-	-	-	-	-	-	-	-
Cu _{2-shell}	55	1045	746,429	0.0076	950,950	0.0086	1.0
Cu _{3-shell}	147	2793	1,289,759	0.08	1,912,201	0.04	2.0
Cu _{4-shell}	309	5871	2,047,417	0.39	3,399,083	0.13	3.1
Cu _{5-shell}	561	10659	3,056,521	1.45	5,516,293	0.34	4.3
Cu _{6-shell}	923	17537	4,352,211	4.74	8,439,912	0.93	5.1

TABLE III: Computational cost (η_c) comparison between PAW-FE with QE in node-hrs with both solved to achieve $\sim 2 \times 10^{-4}$ Ha/atom discretization error. Computational cost is computed as product of number of nodes and τ_c .

Case Study: Performance benchmarking study on Cu nanoclusters

of finite-element basis allows the FE mesh to be coarse-grained into the vacuum in contrast to a uniform spatial resolution of the plane-wave basis in QE, which is also a key factor for the superior gains observed in PAW-FE. Finally, the Table IV compares the average time per SCF in terms of minimum wall time (τ_c^{\min}) obtained in both PAW-FE and QE. We note that the minimum wall time of QE is measured at $\sim 30\% - 40\%$ scaling efficiency while a scaling efficiency of $\sim 50\% - 55\%$ is reached for PAW-FE⁴. Even for a small system involving Cu_{3-shell} com-

prising of 2793 electrons, we observe a gain of around $3.2\times$ in the minimum wall time for PAW-FE compared to QE, and we see almost a staggering speed up of $10\times$ for Cu_{6-shell} comprising of 17,537 electrons, the largest system considered in this study. The increased speedup with system sizes is attributed to the superior scaling of PAW-FE which requires only nearest neighbour communication and the various efficient computational methodologies employed in solving the PAW eigenvalue problem using the Chebyshev filtered subspace iteration approach (ChFSI) in PAW-FE (see Section IV).

System	QE (τ_c^{\min}) sec	PAW-FE (τ_c^{\min}) sec	Speed-up
-	-	-	-
Cu _{3-shell}	31.2	9.8	3.2
Cu _{4-shell}	96.3	15.5	6.2
Cu _{5-shell}	150.7	20.9	7.2
Cu _{6-shell}	490.0	48.6	10.1

TABLE IV: Minimum wall time per SCF comparison (τ_c^{\min}) between PAW-FE with QE to achieve a discretization error of $\sim 2 \times 10^{-4}$ Ha/atom. **Case Study:** Performance benchmarking study on Cu nanoclusters

B. Periodic/Semi-periodic systems

In this subsection, we consider the case of periodic and semi-periodic systems for our accuracy and performance benchmarking. In particular, we benchmark the accuracy of PAW-FE with ABINIT by comparing energy versus lattice parameters of representative bulk systems involving Li₂O, Cu, Cu₃Pt and Li unit cells. Further, we compute and benchmark with ABINIT the formation energy of Li₂O and the surface energies of the semi-periodic systems – Zr(001) and La(011) terminated Lithium Lan-

thanum Zirconium Oxide (LLZO), an electrolyte material. Finally, we compare the band structure of C diamond primitive cell obtained from PAW-FE and ABINIT. Following the accuracy benchmarking study, we assess the performance of PAW-FE with QE on two metrics (η_c , τ_c^{\min}) on increasing sizes of Cu₃Pt supercells.

1. Accuracy benchmarking

In all the accuracy benchmarking studies of periodic/semi-periodic systems reported here, we compute the all-electron PAW ground state energy using Eqn. (38) in PAW-FE. Further, we choose refined finite-element (FE) meshes with FE interpolating polynomial degree to be 7 and the mesh size h to be around 1.0 Bohr while in the case of ABINIT, we use a plane-wave cut-off energy $E_{\text{cut}}^{\text{wfc}} = 60$ Ha.

a. Energy vs lattice parameter: Figure (2) shows the variation of ground-state energy as a function of lattice parameter for the case Li₂O(cubic), Cu(fcc), Cu₃Pt(fcc) and Li(bcc) unitcells. We use orthogonal unit-cells in each case and employ shifted $8 \times 8 \times 8$ Monkhorst-Pack k-point grid for sampling the Brillouin zone [92]. In Fig.(2), we plot the energies relative to the minimum ground-state energy obtained in this study using PAW-FE and ABINIT for each of the above material systems. This is done to account for different energy scales in the two implementations considered here. From Fig.(2), we observe

⁴ PAW-FE could be scaled further on more nodes, the restriction of 140 high-memory nodes on PARAM-Pravega limits the further reduction of minimum wall time

System	Crystal type	Lattice parameter (Bohr) PAW-FE	Lattice parameter (Bohr) ABINIT
Li ₂ O	cubic	8.76	8.76
Li	bcc	6.50	6.50
Cu ₃ Pt	fcc	7.04	7.04
Cu	fcc	6.85	6.85

TABLE V: Comparison of lattice parameters at the minimum energy configuration between ABINIT and PAW-FE for Li₂O(cubic), Li(bcc), Cu₃Pt(fcc) and Cu(fcc) unit-cells obtained from Fig.(2).

an excellent correspondence between PAW-FE and ABINIT. Furthermore, we also observe from Table. V that the lattice parameters at the minimum energy configurations show an excellent match for all the representative periodic systems considered here.

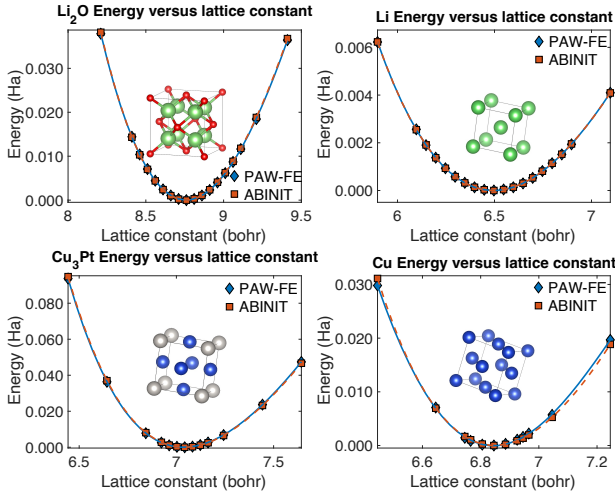


FIG. 2: Comparison between ABINIT and PAW-FE : Energy vs lattice parameter for (a) Li₂O cubic, (b) Li bcc, (c) Cu₃Pt fcc (d) Cu fcc unit-cells. The energy shown is relative to the minimum ground-state energy obtained in each code.

b. Formation energy: Using the ground-state energies at the minimum energy configuration obtained from Fig. 2, we compute the formation energy $\Delta E_f^{\text{Li}_2\text{O}}$ of Li₂O as Hartree-per-formula unit(Ha/f.u.) using the following expression:

$$\Delta E_f^{\text{Li}_2\text{O}} = \frac{1}{4} E_{\text{Li}_2\text{O}} - E_{\text{Li}} - \frac{1}{2} E_{\text{O}_2} \quad (53)$$

To this end, $\Delta E_f^{\text{Li}_2\text{O}}$ is found to be -0.223095 Ha/f.u. in ABINIT, while in the case of PAW-FE, we obtain a value of -0.223126 Ha/f.u. This results in a difference of $\sim 3.2 \times 10^{-5}$ Ha/f.u., establishing a good agreement in the formation energy computed between the two codes

	ABINIT	PAW-FE
System	Surface Energy (J/m ²)	Surface Energy (J/m ²)
La(011)	0.925	0.924
Zr(001)	1.737	1.735

TABLE VI: Comparison of LLZO surface energy computed using PAW-FE with semi-periodic boundary conditions and ABINIT with periodic boundary conditions. La(011) and Zr(001) surfaces are considered in this study with the Zr(001) surface being of higher energy. The difference in surface energy between the two codes is $\sim 2 \times 10^{-3} \text{ J/m}^2$.

c. Surface energies: Next, we compute and validate the surface energies of LLZO (*Lithium Lanthanum Zirconium Oxide*), a material of interest for solid electrolytes, focusing on La(011) and Zr(001) terminations. We obtain the coordinates from a study of LLZO particle morphology[93]. The slab is placed at the center of the simulation domain with 25 Bohr vacuum on either side. In PAW-FE, semi-periodic boundary conditions are employed for the electronic fields, with homogeneous Dirichlet boundary conditions for $\varphi^h(\mathbf{x})$ on the boundary parallel to the surface. While in ABINIT, periodic boundary conditions are employed. The surface energy(γ) is computed using the following expression in the units of J/m²

$$\gamma = \frac{1}{2A_{\text{surface}}} (E_{\text{surface}} - E_{\text{bulk}}) \quad (54)$$

where A_{surface} is the surface area, E_{surface} is the ground-state (GS) energy of the material systems with the surface of interest and E_{bulk} is the GS energy of the corresponding bulk system and the values obtained from PAW-FE and ABINIT are shown in Table VI. From this table, we observe a close match in surface energies computed from both codes. The difference in surface energies are $\sim 2 \times 10^{-3} \text{ J/m}^2$. Additionally, it is observed that the Zr(001) surface has higher surface energy in both codes, consistent with observations from previous studies[93].

d. Band structure comparisons: We now compute the band-structure of the diamond primitive cell of Carbon with lattice constant 3.373 Bohr. The Brioullin Zone(BZ) and the k-point path are shown in Fig.(3) and were obtained using seeK-path[94]. A shifted $8 \times 8 \times 8$ Monkhorst-Pack k-point grid was used for the initial SCF calculation for sampling the Brillouin zone, following which a non-self-consistent field (NSCF) calculation was performed using the k-points specified along the high symmetry points of Fig.(3) to extract the band structure. Figure (3) shows the overlay of the band structure computed using ABINIT and PAW-FE. We observe an excellent match in the eigenvalues and, hence, the band structure between the two codes.

Cu ₃ Pt Supercell	electrons	QE #basis	QE(η_c) Node-hrs	PAW-FE #basis	PAW-FE(η_c) Node-hrs	Ratio
-	-	-	-	-	-	-
$4 \times 4 \times 4$	4288	128,923	0.02	753,571	0.03	0.5
$5 \times 5 \times 5$	8375	251,727	0.113	1,520,875	0.091	1.23
$6 \times 6 \times 6$	14472	434,257	0.51	2,685,619	0.3	1.7
$7 \times 7 \times 7$	22981	690,981	1.84	4,330,747	0.79	2.3
$8 \times 8 \times 8$	34304	1,032,445	6.16	5,929,741	1.92	3.2

TABLE VII: Computational cost (η_c) comparison of PAW-FE with QE. The table compares computational cost in Node-hrs and number of basis functions to achieve $\sim 2 \times 10^{-4}$ Ha/atom discretization error. Computational cost is computed as product of number of nodes and τ_c . The calculations were performed on HM nodes of Param Pravega supercomputer. **Case Study:** Periodic performance benchmarking study on Cu₃Pt supercells

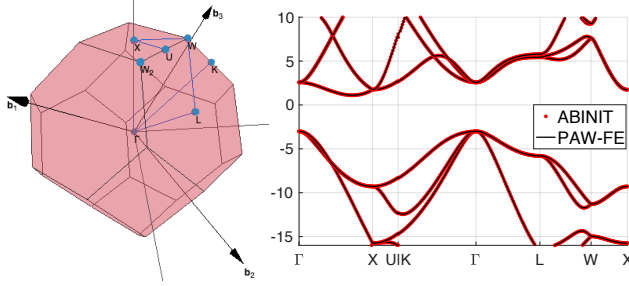


FIG. 3: Band structure comparison between ABINIT and PAW-FE. The left figure shows the k-path used to generate the band structure while the right compares the band structure between ABINIT (red) and PAW-FE (black). **Case Study:** Carbon diamond primitive cell

The comprehensive benchmarking studies discussed here establish the accuracy of our PAW-FE computational methodology and implementation for periodic/semi-periodic systems. We now proceed to discuss performance aspects of PAW-FE for periodic systems with increasing system sizes.

2. Performance benchmarking

We benchmark here the performance of PAW-FE with QE similar to the non-periodic systems discussed previously and compare the computational efficiency and minimum wall time on increasingly large supercells of Cu₃Pt crystal solved to similar levels of accuracy between the two approaches. The supercells are constructed by stacking of Cu₃Pt unit cells along the three lattice dimensions and to this end, we consider supercells of sizes $4 \times 4 \times 4$ (4288 electrons), $5 \times 5 \times 5$ (8375 electrons), $6 \times 6 \times 6$ (14472 electrons), $7 \times 7 \times 7$ (22981 electrons), $8 \times 8 \times 8$ (34304

electrons). We perform a Γ -point calculation with periodic boundary conditions imposed on all electronic fields in both PAW-FE and QE. The discretization parameters employed in PAW-FE are $p = 6$, $h = 1.8$ Bohr while in the case of QE $E_{\text{cut}}^{\text{wfc}} = 25$ Ha is used to achieve a discretization error of $2 \times 10^{-4} \frac{\text{Ha}}{\text{atom}}$.

Table(VII) and Table(VIII) presents the computational cost and minimum wall time comparison between PAW-FE and QE. We recall that the computational cost (η_c) is computed as the product of minimum number of nodes required to fit the problem and the average wall time per SCF iteration. From the Table.(VII), we observe that the number of basis functions required by PAW-FE is a factor of $6\times$ higher than QE and we begin to see computational gains in PAW-FE for systems greater than 8000 electrons. The efficiency gains we achieve with an increase in system sizes are around $1.7\times$, $2.3\times$ and $3.2\times$ for $6 \times 6 \times 6$, $7 \times 7 \times 7$, $8 \times 8 \times 8$ Cu₃Pt supercells respectively, the benchmark systems considered for CPU-time comparison. We note that the gains obtained in the periodic case are lesser than the case of non-periodic systems because of the degrees of freedom advantage that plane-wave (PW) codes provide for bulk systems (~ 500 PW basis functions per atom) compared to non-periodic systems (~ 5000 PW basis functions per atom) to reach the desired accuracy. However, we still see an increase in computational gains for PAW-FE compared to QE as the system size increases due to the requirement of the higher number of nodes to fit larger problems that can affect the parallel scalability of QE compared to PAW-FE. Finally, the Table(VIII) compares the average time per SCF in terms of minimum wall time (τ_c^{min}) between PAW-FE and QE. To this end, we observe a gain of around $2.3\times$ for Cu₃Pt $5 \times 5 \times 5$ supercell with 8375 electrons and the computational gains increase to almost $7.7\times$ for system size comprising of 34304 electrons. Even for fully periodic calculations, these increased gains with system size underscore the importance of fast and scalable computational methods developed in this work.

C. Scalability and parallel efficiency

In this subsection, we compare the computational cost and parallel scaling efficiency of PAW-FE relative to the

pseudopotential implementation in DFT-FE using the optimized norm-conserving vanderbilt (ONCV) pseudopo-

Cu ₃ Pt Supercell	QE (τ_c^{\min})	PAW-FE (τ_c^{\min})	Speed-up
-	sec	sec	-
$5 \times 5 \times 5$	42.1	18	2.3
$6 \times 6 \times 6$	96.7	26.8	3.61
$7 \times 7 \times 7$	282.9	45.7	6.2
$8 \times 8 \times 8$	836.1	109	7.67

TABLE VIII: Min wall time comparison of PAW-FE with QE with discretization error of $\sim 2 \times 10^{-4}$ Ha/atom. **Case Study:** Periodic performance benchmarking study on Cu₃Pt supercells

tentials [95]. Towards this, we consider $9 \times 9 \times 9$ Cu₃Pt supercell and Pt₂₀₅₇ nanocluster as representative systems for periodic and non-periodic calculations. We obtain the PAW data-set and ONCV pseudopotential data from pseudodojo[88, 89] repository. The FE-discretization parameters is determined such that the difference in ground-state energies between successive subdivided meshes are 2×10^{-4} Ha/atom. Table (IX) shows the differences in FE-discretization parameters, number of electrons and number of basis functions between the ONCV based DFT-FE and PAW-FE calculations. We compute the average time per SCF τ_c as discussed in the beginning of this section. The simulations for this study were run on Frontier ⁵CPUs.

The strong scaling results are shown in Fig.(4). The minimum nodes for Cu₃Pt requires 60 nodes for ONCV and 8 nodes for PAW calculation with ~ 20 k DoFs/task. Similarly, for the nonperiodic system Pt₂₀₅₇ nanocluster the ONCV simulation required 100 nodes while the PAW simulation required 25 nodes with ~ 15 k DoFs/task. From fig.(4) we observe that for the periodic system PAW-FE is $10\times$ more efficient than ONCV based DFT-FE. Moreover, the parallel scalability of PAW-FE similar to that of DFT-FE. The gain in computational efficiency of PAW-FE can be attributed to two main reasons: (i) requirement of $\sim 8\times$ more nodes for DFT-FE to run ONCV calculations due to higher peak memory demand which resulted in reduced scaling efficiency and (ii) reduced Chebyshev polynomial degrees from 50 in ONCV to 20 in PAW-FE simulation. Similarly for the nonperiodic study we observe $12\times$ gain in computational efficiency of PAW-FE over DFT-FE. Further we observe that the parallel scaling efficiency of PAW-FE is better than DFT-FE. The reasons for the efficiency gain is similar to that of the periodic system. Additionally, the gain in parallel scaling efficiency is due higher electrons in the ONCV calculation increasing the Rayleigh-Ritz(RR) cost which scales as $O(MN_e^2)$.

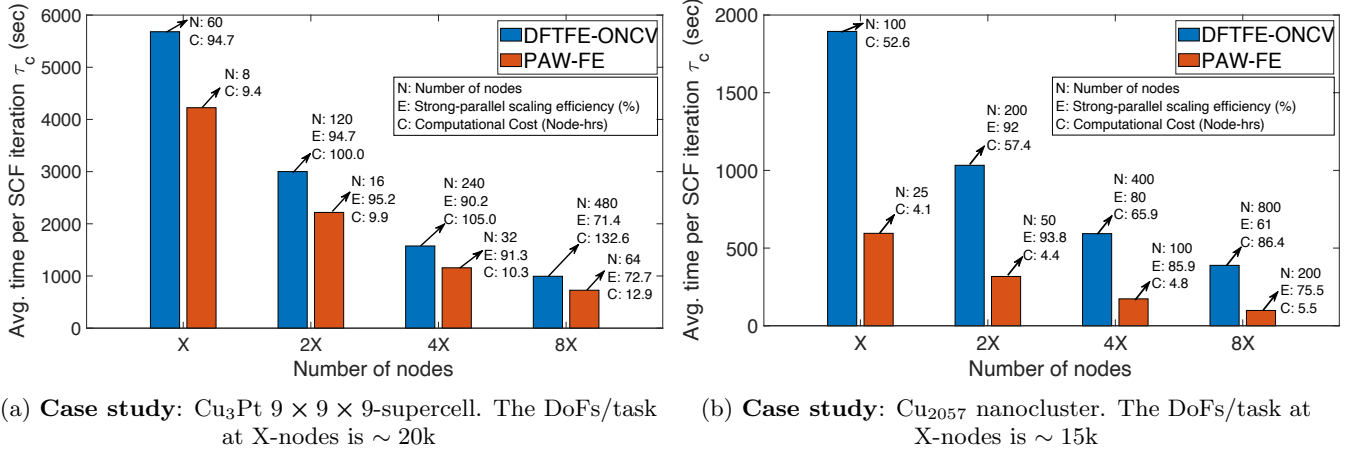


FIG. 4: Comparison of ONCV pseudopotential DFT-FE against PAW-FE on Frontier CPUs. The figures compares the average wall time per SCF, scaling efficiency, computational cost between DFT-FE and PAW-FE for $9 \times 9 \times 9$ Cu₃Pt supercell and Pt₂₀₅₇ nanocluster

VI. CONCLUSIONS

In this work we present for the first time a local real-space formulation of the PAW method that is amenable for finite element(FE) discretization(PAW-FE). This work demonstrates the computational advan-

⁵ Frontier is the worlds fastest exascale computer. Each compute node of Frontier has 64 core AMD Epyc 7713 processor with 512 GB memory and multiple slingshot NICs for communication between nodes.

System	-	ONCV	PAW
Cu ₃ Pt	No of electrons(N_e)	54,685	48,933
	p, p_{el}, h	6, 6, 0.92 Bohr	6, 7, 1.85 Bohr
	No. of basis/atom	23,463	2,954
Pt ₂₀₅₇	No. of electrons(N_e)	37,026	20,570
	p, p_{el}, h	6, 6, 0.85 Bohr	5, 7, 1.2 Bohr
	No. of basis/atom	41,031	10,306

TABLE IX: Comparison of ONCV based DFT-FE and PAW-FE on periodic(Cu₃Pt) and nonperiodic(Pt₂₀₅₇) systems

tage over the current state-of-the-art plane wave methods for medium to large-scale systems and thereby pushing the boundaries of length-scales that can be realised from ab-initio calculations than possible today.

The development of the proposed method relies on the culmination of the following five main ideas. First, the local real-space reformulation of Blöchl’s PAW electrostatics evaluation thereby making it feasible for finite element discretization. Second, we employed higher order quadrature rules to efficiently and accurately evaluate integrals involving atom-centered functions, thereby allowing the use of coarser FE grids for the electronic fields. Third, we implemented a self consistent field(SCF) iteration approach based on the Anderson mixing of total charge density involving the smooth electron density $\tilde{n}(\mathbf{x})$ and atom centered occupation matrix $\{\mathbf{D}^a\}$. Furthermore, the local real-space formulation of the weighted residual norm enables an efficient evaluation for the mixing procedure. Fourth, we developed an efficient scheme to evaluate the inverse of FE discretized PAW overlap matrix \mathbf{S} . Finally, we leveraged the efficient computation of \mathbf{S}^{-1} to design a Chebyshev polynomial based filter in each SCF iteration to compute the occupied eigenspace. Here, we leverage the FE-cell-level structure of the discretized Hamiltonian(\mathbf{H}) and the inverse paw overlap(\mathbf{S}^{-1}) matrix to design computationally efficient strategies that minimise peak memory requirement while using cache friendly matrix-matrix products to evaluate the action of the Chebyshev filter on the subspace.

The accuracy of the proposed method was validated against plane-wave (PW) code across various non-periodic, semi-periodic, and fully periodic representative systems. Compared to the PW calculations, our implementation showed excellent agreement in ground-

state energies, energy variation with bond length and lattice parameters, formation energies, surface energies, and band structures. Furthermore, in comparison with state-of-the art PW codes, the efficient computational strategies employed in PAW-FE enabled a $5\times$ reduction in computational cost in nonperiodic systems(~ 18000 electrons) and a $3\times$ in periodic systems (~ 34000 electrons) with greater reductions observed as system size increases. The minimum wall time reason ... Additionally, PAW-FE exhibits excellent parallel scaling efficiency ($\sim 70\%$) at 1200 degrees of freedom per MPI task and achieves a substantial ten-fold reduction in computational cost over current state-of-the-art DFT-FE code using norm conserving pseudopotentials for system sizes close to 50000 electrons.

The ability of PAW-FE to handle generic boundary conditions in conjunction with the substantial reduction in computational resource requirement will facilitate ab-initio calculations at larger length scales. This capability, enables the study of complex systems and interfaces feasible by providing a richer energy landscape for robust statistical and ML based computational models. Additionally, we plan to extend the current CPU implementation of PAW-FE to leverage GPU accelerators, thereby achieving a significant reduction in time to solution.

talk about generating better landscape for ML potentials, understand interphases

VII. ACKNOWLEDGEMENTS

The authors would like to thank Prof. Vikram Gavini for many helpful discussions and his valuable suggestions. The authors gratefully acknowledge the seed grant from Indian Institute of Science and SERB Startup Research Grant from the Department of Science and Technology India (Grant Number: SRG/2020/002194) for the purchase of a GPU cluster, which also provided computational resources for this work. The research used the resources of PARAM Pravega at Indian Institute of Science, supported by National Supercomputing Mission (NSM) R&D for exa-scale grant (DST/NSM/R&D Exascale/2021/14.02). K.R. would like to acknowledge Prime Minister Research Fellowship(PMRF) from the Ministry of Education India for financial support. S.D would like to thank TRI.

[1] P. Hohenberg and W. Kohn, Inhomogeneous electron gas, Phys. Rev. **136**, B864 (1964).
[2] W. Kohn and L. J. Sham, Self-consistent equations including exchange and correlation effects, Phys. Rev. **140**, A1133 (1965).
[3] G. B. Bachelet, D. R. Hamann, and M. Schlüter, Pseudopotentials that work: From h to pu, Phys. Rev. B **26**, 4199 (1982).

[4] J. R. Chelikowsky, The pseudopotential-density functional method applied to nanostructures, Journal of Physics D: Applied Physics **33**, R33 (2000).
[5] P. Schwerdtfeger, The pseudopotential approximation in electronic structure theory, ChemPhysChem **12**, 3143 (2011).
[6] D. R. Hamann, M. Schlüter, and C. Chiang, Norm-conserving pseudopotentials, Phys. Rev. Lett. **43**, 1494 (1979).

- [7] D. Vanderbilt, Optimally smooth norm-conserving pseudopotentials, *Phys. Rev. B* **32**, 8412 (1985).
- [8] D. R. Hamann, Generalized norm-conserving pseudopotentials, *Phys. Rev. B* **40**, 2980 (1989).
- [9] N. Troullier and J. L. Martins, Efficient pseudopotentials for plane-wave calculations, *Phys. Rev. B* **43**, 1993 (1991).
- [10] D. Vanderbilt, Soft self-consistent pseudopotentials in a generalized eigenvalue formalism, *Phys. Rev. B* **41**, 7892 (1990).
- [11] P. E. Blöchl, Projector augmented-wave method, *Phys. Rev. B* **50**, 17953 (1994).
- [12] L. Kronik, A. Makmal, M. L. Tiago, M. M. G. Alemany, M. Jain, X. Huang, Y. Saad, and J. R. Chelikowsky, PARSEC — the pseudopotential algorithm for real-space electronic structure calculations: recent advances and novel applications to nano-structures, *Phys. Status Solidi B* **243**, 1063 (2006).
- [13] V. Michaud-Rioux, L. Zhang, and H. Guo, RESCU: A real space electronic structure method, *J. Comput. Phys.* **307**, 593 (2016).
- [14] S. Ghosh and P. Suryanarayana, SPARC: Accurate and efficient finite-difference formulation and parallel implementation of density functional theory: Isolated clusters, *Comput. Phys. Commun.* **212**, 189 (2017).
- [15] X. Andrade, D. Strubbe, U. De Giovannini, A. H. Larsen, M. J. T. Oliveira, J. Alberdi-Rodriguez, A. Varas, I. Theophilou, N. Helbig, M. J. Verstraete, L. Stella, F. Nogueira, A. Aspuru-Guzik, A. Castro, M. A. L. Marques, and A. Rubio, Real-space grids and the Octopus code as tools for the development of new simulation approaches for electronic systems, *Phys. Chem. Chem. Phys.* **17**, 31371 (2015).
- [16] J. Enkovaara, C. Rostgaard, J. J. Mortensen, J. Chen, M. Dulak, L. Ferrighi, J. Gavnholt, C. Glinsvad, V. Haikola, H. A. Hansen, H. H. Kristoffersen, M. Kuisma, A. H. Larsen, L. Lehtovaara, M. Ljungberg, O. Lopez-Acevedo, P. G. Moses, J. Ojanen, T. Olsen, V. Petzold, N. A. Romero, J. Stausholm-Møller, M. Strange, G. A. Tritsarlis, M. Vanin, M. Walter, B. Hammer, H. Häkkinen, G. K. H. Madsen, R. M. Nieminen, J. K. Nørskov, M. Puska, T. T. Rantala, J. Schiøtz, K. S. Thygesen, and K. W. Jacobsen, Electronic structure calculations with GPAW: a real-space implementation of the projector augmented-wave method, *J. Phys. Condens. Matter* **22**, 253202 (2010).
- [17] E. Tsuchida and M. Tsukada, Electronic-structure calculations based on the finite-element method, *Phys. Rev. B* **52**, 5573 (1995).
- [18] E. Tsuchida and M. Tsukada, Adaptive finite-element method for electronic-structure calculations, *Phys. Rev. B* **54**, 7602 (1996).
- [19] J. E. Pask, B. M. Klein, C. Y. Fong, and P. A. Sterne, Real-space local polynomial basis for solid-state electronic-structure calculations: A finite-element approach, *Phys. Rev. B* **59**, 12352 (1999).
- [20] J. E. Pask and P. A. Sterne, Finite element methods in ab initio electronic structure calculations, *Modell. Simul. Mater. Sci. Eng.* **13**, R71 (2005).
- [21] E. J. Bylaska, M. Holst, and J. H. Weare, Adaptive finite element method for solving the exact Kohn-Sham equation of density functional theory, *J. Chem. Theory. Comput.* **5**, 937 (2009).
- [22] P. Suryanarayana, V. Gavini, T. Blesgen, K. Bhattacharya, and M. Ortiz, Non-periodic finite-element formulation of Kohn-Sham density functional theory, *J. Mech. Phys. Solids* **58**, 256 (2010).
- [23] P. Motamarri, M. Nowak, K. Leiter, J. Knap, and V. Gavini, Higher-order adaptive finite-element methods for kohn-sham density functional theory, *Journal of Computational Physics* **253**, 308 (2013).
- [24] V. Schauer and C. Linder, All-electron Kohn-Sham density functional theory on hierarchic finite element spaces, *J. Comput. Phys.* **250**, 644 (2013).
- [25] H. Chen, X. Dai, X. Gong, L. He, and A. Zhou, Adaptive finite element approximations for Kohn-Sham models, *Multiscale Model. Simul.* **12**, 1828 (2014).
- [26] D. Davydov, T. D. Young, and P. Steinmann, On the adaptive finite element analysis of the Kohn-Sham equations: methods, algorithms, and implementation, *Int. J. Numer. Methods Eng.* **106**, 863 (2016).
- [27] B. Kanungo and V. Gavini, Large-scale all-electron density functional theory calculations using an enriched finite-element basis, *Phys. Rev. B* **95**, 035112 (2017).
- [28] B. Kanungo and V. Gavini, Real time time-dependent density functional theory using higher order finite-element methods, *Phys. Rev. B* **100**, 115148 (2019).
- [29] P. Motamarri, S. Das, S. Rudraraju, K. Ghosh, D. Davydov, and V. Gavini, Dft-fe – a massively parallel adaptive finite-element code for large-scale density functional theory calculations, *Computer Physics Communications* **246**, 106853 (2020).
- [30] S. Das, P. Motamarri, V. Gavini, B. Turcksin, Y. W. Li, and B. Leback, Fast, Scalable and Accurate Finite-Element Based Ab Initio Calculations Using Mixed Precision Computing: 46 PFLOPS Simulation of a Metallic Dislocation System, in *Proceedings of the International Conference for High Performance Computing, Networking, Storage and Analysis*, Vol. 11 (ACM, New York, NY, USA, 2019) pp. 1–11.
- [31] L. Genovese, A. Neelov, S. Goedecker, T. Deutsch, S. A. Ghasemi, A. Willand, D. Caliste, O. Zilberberg, M. Rayson, A. Bergman, and R. Schneider, Daubechies wavelets as a basis set for density functional pseudopotential calculations, *The Journal of Chemical Physics* **129**, 014109 (2008).
- [32] L. Genovese, M. Ospici, T. Deutsch, J.-F. Méhaut, A. Neelov, and S. Goedecker, Density functional theory calculation on many-cores hybrid central processing unit-graphic processing unit architectures, *The Journal of Chemical Physics* **131**, 034103 (2009).
- [33] S. Mohr, L. E. Ratcliff, P. Boulanger, L. Genovese, D. Caliste, T. Deutsch, and S. Goedecker, Daubechies wavelets for linear scaling density functional theory, *The Journal of Chemical Physics* **140**, 204110 (2014).
- [34] W. Hu, L. Lin, and C. Yang, DGDF: A massively parallel method for large scale density functional theory calculations, *J. Chem. Phys.* **143**, 124110 (2015).
- [35] P. Motamarri and V. Gavini, Tucker-tensor algorithm for large-scale Kohn-Sham density functional theory calculations, *Phys. Rev. B* **93**, 035111 (2017).
- [36] Q. Xu, P. Suryanarayana, and J. E. Pask, Discrete discontinuous basis projection method for large-scale electronic structure calculations, *J. Chem. Phys.* **149**, 094104 (2018).
- [37] C.-C. Lin, P. Motamarri, and V. Gavini, Tensor-structured algorithm for reduced-order scaling large-scale

- Kohn–Sham density functional theory calculations, npj Comput. Mater. **7**, 50 (2021).
- [38] C.-C. Lin and V. Gavini, TTDFT: A GPU accelerated Tucker tensor DFT code for large-scale Kohn-Sham DFT calculations, arXiv:2110.15853 (2021) (2021).
- [39] G. Panigrahi, N. Kodali, D. Panda, and P. Motamarri, Fast hardware-aware matrix-free algorithm for higher-order finite-element discretized matrix multivector products on distributed systems (2023), arXiv:2208.07129 [physics.comp-ph].
- [40] S. Das, B. Kanungo, V. Subramanian, G. Panigrahi, P. Motamarri, D. Rogers, P. Zimmerman, and V. Gavini, Large-scale materials modeling at quantum accuracy: Ab initio simulations of quasicrystals and interacting extended defects in metallic alloys, in *Proceedings of the International Conference for High Performance Computing, Networking, Storage and Analysis*, SC '23 (Association for Computing Machinery, New York, NY, USA, 2023).
- [41] K. Ghosh, H. Ma, M. Onizhuk, V. Gavini, and G. Galli, Spin–spin interactions in defects in solids from mixed all-electron and pseudopotential first-principles calculations, npj Comput. Mater. **7**, 123 (2021).
- [42] S. Das, P. Motamarri, V. Subramanian, D. M. Rogers, and V. Gavini, Dft-fe 1.0: A massively parallel hybrid cpu-gpu density functional theory code using finite-element discretization, Computer Physics Communications **280**, 108473 (2022).
- [43] R. Zhuravel, H. Huang, G. Polycarpou, S. Polydorides, P. Motamarri, L. Katrivas, D. Rotem, J. Sperling, L. A. Zotti, A. B. Kotlyar, J. C. Cuevas, V. Gavini, S. S. Skourtis, and D. Porath, Backbone charge transport in double-stranded dna, Nature Nanotechnology **15**, 836 (2020).
- [44] V. Menon, S. Das, V. Gavini, and L. Qi, Atomistic simulations and machine learning of solute grain boundary segregation in mg alloys at finite temperatures, Acta Materialia **264**, 119515 (2024).
- [45] P. Kumar, M. M. Ludhwani, S. Das, V. Gavini, A. Kanjarla, and I. Adlakha, Effect of hydrogen on plasticity of α -fe: A multi-scale assessment, International Journal of Plasticity **165**, 103613 (2023).
- [46] M. F. Shojaei, J. Holber, S. Das, G. Teichert, T. Mueller, L. Hung, V. Gavini, and K. Garikipati, Bridging scales with machine learning: From first principles statistical mechanics to continuum phase field computations to study order–disorder transitions in lixcoo2, Journal of the Mechanics and Physics of Solids **190**, 105726 (2024).
- [47] L. Yao, S. Das, X. Liu, K. Wu, Y. Cheng, V. Gavini, and B. Xiao, Modulating the microscopic lattice distortions through the al-rich layers for boosting the ferroelectricity in al: Hfo2 nanofilms, Journal of Physics D: Applied Physics **55**, 455501 (2022).
- [48] K. Ghosh, H. Ma, V. Gavini, and G. Galli, All-electron density functional calculations for electron and nuclear spin interactions in molecules and solids, Phys. Rev. Mater. **3**, 043801 (2019).
- [49] B. Kanungo, P. M. Zimmerman, and V. Gavini, Exact exchange-correlation potentials from ground-state electron densities, Nature Communications **10**, 4497 (2019).
- [50] G. Kresse and D. Joubert, From ultrasoft pseudopotentials to the projector augmented-wave method, Phys. Rev. B **59**, 1758 (1999).
- [51] M. Torrent, F. Jollet, F. Bottin, G. Zerah, and X. Gonze, Implementation of the projector augmented-wave method in the abinit code: Application to the study of iron under pressure, Computational Materials Science **42**, 337 (2008).
- [52] M. Torrent, N. Holzwarth, F. Jollet, D. Harris, N. Lepley, and X. Xu, Electronic structure packages: Two implementations of the projector augmented wave (paw) formalism, Computer Physics Communications **181**, 1862 (2010).
- [53] P. Giannozzi, S. Baroni, N. Bonini, M. Calandra, R. Car, C. Cavazzoni, D. Ceresoli, G. L. Chiarotti, M. Cococcioni, I. Dabo, A. D. Corso, S. de Gironcoli, S. Fabris, G. Fratesi, R. Gebauer, U. Gerstmann, C. Gougousis, A. Kokalj, M. Lazzeri, L. Martin-Samos, N. Marzari, F. Mauri, R. Mazzarello, S. Paolini, A. Pasquarello, L. Paulatto, C. Sbraccia, S. Scandolo, G. Sclauzero, A. P. Seitsonen, A. Smogunov, P. Umari, and R. M. Wentzcovitch, Quantum espresso: a modular and open-source software project for quantum simulations of materials, J. Phys.: Condens. Matter **21**, 395502 (2009).
- [54] P. E. Blöchl, C. J. Först, and J. Schimpl, Projector augmented wave method: ab initio molecular dynamics with full wave functions, Bulletin of Materials Science **26**, 33 (2003).
- [55] A. Tackett, N. Holzwarth, and G. Matthews, A projector augmented wave (paw) code for electronic structure calculations, partii: pwpaw for periodic solids in a plane wave basis, Computer Physics Communications **135**, 348 (2001).
- [56] J. Enkovaara, C. Rostgaard, J. J. Mortensen, J. Chen, M. Dulak, L. Ferrighi, J. Gavnholt, C. Glinsvad, V. Haikola, H. A. Hansen, H. H. Kristoffersen, M. Kuisma, A. H. Larsen, L. Lehtovaara, M. Ljungberg, O. Lopez-Acevedo, P. G. Moses, J. Ojanen, T. Olsen, V. Petzold, N. A. Romero, J. Stausholm-Møller, M. Strange, G. A. Tritsaridis, M. Vanin, M. Walter, B. Hammer, H. Häkkinen, G. K. H. Madsen, R. M. Nieminen, J. K. Nørskov, M. Puska, T. T. Rantala, J. Schiøtz, K. S. Thygesen, and K. W. Jacobsen, Electronic structure calculations with gpaw: a real-space implementation of the projector augmented-wave method, Journal of Physics: Condensed Matter **22**, 253202 (2010).
- [57] J. J. Mortensen, L. B. Hansen, and K. W. Jacobsen, Real-space grid implementation of the projector augmented wave method, Phys. Rev. B **71**, 035109 (2005).
- [58] T. Rangel, D. Caliste, L. Genovese, and M. Torrent, A wavelet-based projector augmented-wave (paw) method: Reaching frozen-core all-electron precision with a systematic, adaptive and localized wavelet basis set, Computer Physics Communications **208**, 1 (2016).
- [59] N. D. M. Hine, Linear-scaling density functional theory using the projector augmented wave method, Journal of Physics: Condensed Matter **29**, 024001 (2016).
- [60] Y. Saad, *Numerical Methods for Large Eigenvalue Problems* (Society for Industrial and Applied Mathematics, 2011) <https://epubs.siam.org/doi/pdf/10.1137/1.9781611970739>.
- [61] R. G. Parr, S. R. Gadre, and L. J. Bartolotti, Local density functional theory of atoms and molecules, Proceedings of the National Academy of Sciences **76**, 2522 (1979).
- [62] M. F. Finnis, *Interatomic forces in condensed matter*, Vol. 1 (Oxford Series on Materials Mod, 2003).
- [63] D. C. Langreth and M. Mehl, Beyond the local-density approximation in calculations of ground-state electronic properties, Physical Review B **28**, 1809 – 1834 (1983),

- cited by: 958.
- [64] R. M. Martin, *Electronic structure: basic theory and practical methods* (Cambridge university press, 2020).
 - [65] J. P. Perdew, K. Burke, and M. Ernzerhof, Generalized gradient approximation made simple, *Phys. Rev. Lett.* **77**, 3865 (1996).
 - [66] J. Zwanziger, Computation of nmr observables: Consequences of projector-augmented wave sphere overlap, *Solid State Nuclear Magnetic Resonance* **80**, 14 (2016).
 - [67] S. Das, M. Iyer, and V. Gavini, Real-space formulation of orbital-free density functional theory using finite-element discretization: The case for al, mg, and al-mg intermetallics, *Phys. Rev. B* **92**, 014104 (2015).
 - [68] V. Gavini, J. Knap, K. Bhattacharya, and M. Ortiz, Non-periodic finite-element formulation of orbital-free density functional theory, *Journal of the Mechanics and Physics of Solids* **55**, 669 (2007).
 - [69] N. W. Ashcroft and N. D. Mermin, *Solid state physics* (Cengage Learning, 2022).
 - [70] S. C. Brenner, *The mathematical theory of finite element methods* (Springer, 2008).
 - [71] T. J. Hughes, *The finite element method: linear static and dynamic finite element analysis* (Courier Corporation, 2012).
 - [72] K. J. Bathe, *Finite Element Procedures* (Prentice Hall International Editions (Prentice Hall International, Englewood Cliffs, 1986).
 - [73] D. G. Anderson, Iterative procedures for nonlinear integral equations, *Journal of the ACM (JACM)* **12**, 547 – 560 (1965), cited by: 630; All Open Access, Bronze Open Access.
 - [74] G. Kresse and J. Furthmüller, Efficient iterative schemes for ab initio total-energy calculations using a plane-wave basis set, *Phys. Rev. B* **54**, 11169 (1996).
 - [75] Y. Zhou, J. R. Chelikowsky, and Y. Saad, Chebyshev-filtered subspace iteration method free of sparse diagonalization for solving the kohn–sham equation, *Journal of Computational Physics* **274**, 770 (2014).
 - [76] Y. Zhou, Y. Saad, M. L. Tiago, and J. R. Chelikowsky, Parallel self-consistent-field calculations via chebyshev-filtered subspace acceleration, *Phys. Rev. E* **74**, 066704 (2006).
 - [77] A. Levitt and M. Torrent, Parallel eigensolvers in plane-wave density functional theory, *Computer Physics Communications* **187**, 98 (2015).
 - [78] S. Ghosh and P. Suryanarayana, Sparc: Accurate and efficient finite-difference formulation and parallel implementation of density functional theory: Extended systems, *Computer Physics Communications* **216**, 109 (2017).
 - [79] K.-H. Liou, C. Yang, and J. R. Chelikowsky, Scalable implementation of polynomial filtering for density functional theory calculation in parsec, *Computer Physics Communications* **254**, 107330 (2020).
 - [80] A. W. Max, Inverting modified matrices, in *Memorandum Rept. 42, Statistical Research Group* (Princeton Univ., 1950) p. 4.
 - [81] H. A. van der Vorst, A generalized lanczos scheme, *Mathematics of Computation* **39**, 559 (1982).
 - [82] M. Kronbichler and K. Kormann, A generic interface for parallel cell-based finite element operator application, *Computers & Fluids* **63**, 135 (2012).
 - [83] J. M. Leone Jr, P. M. Gresho, S. T. Chan, and R. L. Lee, A note on the accuracy of gauss–legendre quadrature in the finite element method, *International Journal for Numerical Methods in Engineering* **14**, 769 (1979).
 - [84] D. Roller, A. M. Rappe, L. Kronik, and O. Hellman, Finite difference interpolation for reduction of grid-related errors in real-space pseudopotential density functional theory, *Journal of Chemical Theory and Computation* **19**, 3889 (2023).
 - [85] W. Bangerth and O. Kayser-Herold, Data structures and requirements for hp finite element software, *ACM Transactions on Mathematical Software* **36**, 1 (2009).
 - [86] X. Gonze, F. Jollet, F. Abreu Araujo, D. Adams, B. Amadon, T. Applencourt, C. Audouze, J.-M. Beuken, J. Bieder, A. Bokhanchuk, E. Bousquet, F. Bruneval, D. Caliste, M. Côté, F. Dahm, F. Da Pieve, M. Delaveau, M. Di Gennaro, B. Dorado, C. Espejo, G. Geneste, L. Genovese, A. Gerossier, M. Giantomassi, Y. Gillet, D. Hamann, L. He, G. Jomard, J. Laflamme Janssen, S. Le Roux, A. Levitt, A. Lherbier, F. Liu, I. Lukačević, A. Martin, C. Martins, M. Oliveira, S. Poncé, Y. Pouillon, T. Rangel, G.-M. Rignanese, A. Romero, B. Rousseau, O. Rubel, A. Shukri, M. Stankovski, M. Torrent, M. Van Setten, B. Van Troeye, M. Verstraete, D. Waroquiers, J. Wiktor, B. Xu, A. Zhou, and J. Zwanziger, Recent developments in the abinit software package, *Computer Physics Communications* **205**, 106 (2016).
 - [87] J. P. Perdew, K. Burke, and M. Ernzerhof, Generalized gradient approximation made simple, *Phys. Rev. Lett.* **77**, 3865 (1996).
 - [88] M. van Setten, M. Giantomassi, E. Bousquet, M. Verstraete, D. Hamann, X. Gonze, and G.-M. Rignanese, The PseudoDojo: Training and grading a 85 element optimized norm-conserving pseudopotential table, *Comput. Phys. Commun.* **226**, 39 (2018).
 - [89] F. Jollet, M. Torrent, and N. Holzwarth, Generation of Projector Augmented-Wave atomic data: A 71 element validated table in the XML format, *Comput. Phys. Commun.* **185**, 1246 (2014).
 - [90] J. M. Rahm and P. Erhart, Beyond magic numbers: Atomic scale equilibrium nanoparticle shapes for any size, *Nano Letters* **17**, 5775 (2017), pMID: 28792765, <https://doi.org/10.1021/acs.nanolett.7b02761>.
 - [91] A. Jain, S. P. Ong, G. Hautier, W. Chen, W. D. Richards, S. Dacek, S. Cholia, D. Gunter, D. Skinner, G. Ceder, and K. a. Persson, The Materials Project: A materials genome approach to accelerating materials innovation, *APL Materials* **1**, 011002 (2013).
 - [92] H. J. Monkhorst and J. D. Pack, Special points for brillouin-zone integrations, *Phys. Rev. B* **13**, 5188 (1976).
 - [93] P. Canepa, J. A. Dawson, G. Sai Gautam, J. M. Statham, S. C. Parker, and M. S. Islam, Particle morphology and lithium segregation to surfaces of the li7la3zr2o12 solid electrolyte, *Chemistry of Materials* **30**, 3019 (2018), <https://doi.org/10.1021/acs.chemmater.8b00649>.
 - [94] Y. Hinuma, G. Pizzi, Y. Kumagai, F. Oba, and I. Tanaka, Band structure diagram paths based on crystallography, *Computational Materials Science* **128**, 140 (2017).
 - [95] D. R. Hamann, Optimized norm-conserving vanderbilt pseudopotentials, *Phys. Rev. B* **88**, 085117 (2013).